BEM theory and CFD for Wind Turbine Aerodynamics

Internship Report

JUR MOURITS

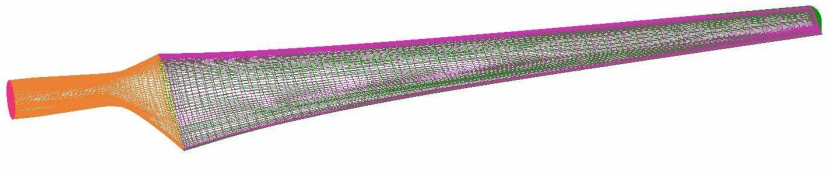

13-01-2014
University of Twente & University of Liverpool

Summary

This project considers an analysis and evaluation of different methods for wind turbine aerodynamics. A Blade Element Momentum method is developed and applied to the Annex XX wind turbine blade. For the sectional data required for this method, 2D CFD simulations are performed with the HMB solver developed by the University of Liverpool. With the use of this BEM method the performance of the wind turbine in terms of thrust, torque and power coefficient is calculated. Besides this also the relative wind angle, angle of incidence and local values of thrust, torque, lift, drag etc., are computed and presented in this report.

Subsequently a 3D grid is build and used to perform 3D CFD simulations of the wind turbine blades. After this, a comparison is made between the BEM method and 3D CFD simulations. For this comparison the University of Liverpool provided results of a more advanced CFD simulations which includes the tower and contains a finer grid. After a comparison of the overall thrust and torque a more detailed analysis is discussed by integrating sectional pressure data.

Finally a sensitivity analyses is performed to investigate the effect of inaccuracies in data and how to deal with this. The discussion explains that BEM methods can predict the performance of a wind turbine quite well without requiring excessive computational power. With the CFD methods, not only the performance of the wind turbine can be predicted very well, but also good insight in the flow behaviour can be provided since the flow around the blade can be visualised.

The work presented in this report is part of a 3 month internship at the CFD lab of the University of Liverpool. The internship is conducted as part of the final year of a master degree in Engineering Fluid Dynamics at the University of Twente.

Nomenclature

a	Axial induction factor
a'	Rotational induction factor
A	Surface Area
α	Angle of Incidence
B	Number of blades
β	Pitch angle
c	Chord
C_A	Normal coefficient defined as $C_A = \frac{F_A}{\frac{1}{2}\rho U^2 A}$
C_D	Drag coefficient defined as $C_D = \frac{D}{\frac{1}{2}\rho U^2 A}$
C_L	Lift coefficient defined as $C_L = \frac{L}{\frac{1}{2}\rho U^2 A}$
C_M	Moment coefficient defined as $C_M = \frac{F_A}{\frac{1}{2}\rho U^2 Ac}$
C_N	Normal coefficient defined as $C_N = \frac{N}{\frac{1}{2}\rho U^2 A}$
C_P	Pressure coefficient defined as $C_P = \frac{P-P_\infty}{\frac{1}{2}\rho U^2}$
C_{pow}	Power coefficient defined as $C_{pow} = \frac{P_{ow}}{\frac{1}{2}\rho U_\infty^3 A}$
C_T	Thrust coefficient wind turbine $C_T = \frac{T}{\frac{1}{2}\rho U_\infty^2 A}$
C_{T-h}	Thrust coefficient helicopters $C_{T-h} = \frac{T}{\frac{1}{2}\rho v_{tip}^2 \pi R^2}$
d_t	Diameter of tower
F_A	Axial force, parallel to chord
λ_r	Speed ratio
λ_t	Tip speed ratio
M	Moment
N	Normal force, perpendicular to chord
$\vec{n}$	Normal vector
Ω	Rotational velocity
ω	Rotational velocity of the flow/wake
$\dot{m}$	Mass flow rate
ϕ	Relative inflow angle
P_{ow}	Power
P	Pressure
P_∞	Free stream pressure
Q	Torque
r	Radial position along the blade
r_0	Radius to begin of blade
r_{sh}	Radius till where the blade experiences the shadow of the tower
ρ	Density
R	Outer radius of the blade
s	Space variable along contour

τ_w	Shear stress at the wall
T	Thrust
θ	Twist angle
U	Velocity
U_∞	Free stream velocity of the wind
U_{rel}	Relative velocity

Contents

Summary **i**

Nomenclature **iii**

Acknowledgements **ix**

1 Introduction **1**

2 Mathematical Models for Rotor Flow Simulations **3**
- 2.1 The Helicopter Multi-Block CFD Solver 3
  - 2.1.1 Vector Form of the Conservation Laws 4
  - 2.1.2 Numerical Methods 5
- 2.2 General Description of Turbulence and its Modelling 7
- 2.3 Reynolds Averaging 7
  - 2.3.1 Time Averaging 8
  - 2.3.2 Spatial Averaging 8
  - 2.3.3 Ensemble Averaging 8
- 2.4 Boussinesq-Based Models 9
- 2.5 Viscosity-Dependent Parameters 10
- 2.6 Two-Equation Models 10
  - 2.6.1 Model Equations: Linear $k - \omega$ Model 11

3 BEM Method **15**
- 3.1 Momentum Theory 15
  - 3.1.1 Axial Momentum Theory 15
  - 3.1.2 Tangential Momentum Theory 17
  - 3.1.3 Blade Element Theory 18
- 3.2 BEM Model 21

4 2D-CFD **25**
- 4.1 The Grid 25
- 4.2 Results 2D-CFD 26
  - 4.2.1 Convergence of the solution 29
  - 4.2.2 Turbulence modelling 33

5 3D-CFD **35**
- 5.1 Annex XX blade 35
- 5.2 The Grid 35
- 5.3 3D-CFD Results 37

6 BEM Results and Comparison with 3D CFD **39**
6.1 Results BEM 39
6.2 Comparison 44
6.3 Comparison by pressure integration 45
6.3.1 Sensitivity Analysis 49

7 Conclusion **53**

List of Figures

3.1 Stream tube with indicated the velocities [30] 16
3.2 Division in annular rings [30] 17
3.3 Tangential momentum concept for in plane forces [30] 18
3.4 Definition of the different angles 19

4.1 2D grid of the S809 airfoil section 25
4.2 Aerodynamic properties of the S809 airfoil section, obtained by the 2D-CFD simulations 26
4.3 Visualisation of the flow around the 2D airfoil 28
4.4 The convergence of the pressure terms of the coefficients 30
4.5 The convergence of the friction terms of the coefficients 31
4.6 Logarithm of the residual of the Navier-Stokes equations 32
4.7 The influence of the different turbulence models on the lift and drag coefficient 33

5.1 Geometric properties of the Annex XX blade 35
5.2 Topology of the 3D grid 36
5.3 The cells of the grid at the surface of the blade 36
5.4 A slice of the grid zoomed in on the airfoil section 37
5.5 The streamlines at the upper surface obtained by 3D simulations . . . 37

6.1 The induction factors compared to the Betz limit 40
6.2 The convergence of induction factor a at r = 1.25 m 40
6.3 The geometric angles compared with the different definition of the inflow angles 41
6.4 The sectional C_l and the components in thrust and torque direction . . 41
6.5 The forces and torque along the radius 42
6.6 The sectional power coefficient C_{pow} 43
6.7 The thrust per blade with the tower shadow model 44
6.8 The torque with including the tower shadow effects 45
6.9 Integration of the pressure coefficient 45
6.9 Comparison of the sectional C_p curves 48
6.9 The different coefficients at the sections at 30%, 46%, 63%, 80% and 95% obtained by the different methods 50

6.10 The sensitivity of the torque and thrust 51

7.1 C_p values for $\frac{r}{R} = 30\%$ 60
7.2 C_p difference upper surface 61

List of Tables

2.1 Different types of two-equation turbulence models and the corresponding second variable. 11
2.2 Different types of linear $k - \omega$ turbulence models 12
2.3 Values of constants used in linear $k - \omega$ models. 13

6.1 BEM results for $U_\infty = 7$ m/s and $\Omega = 72$ rpm 42

Acknowledgements

I would like to express my great appreciation to Professor G.N. Barakos and Dr. R. Steijl for supervising me during this project. The discussions were very helpful and I am very grateful for the way Professor G.N. Barakos and Dr. R. Steijl were always willing to help me and to answer my questions.Their comments and advises were very useful and instructive. I would like to thank Professor H. W. M. Hoeijmakers for the supervision on behalf of the University of Twente. His help in finding a placement and the assistance during the project itself was greatly appreciated. I would also like to thank the staff of the CFD-laboratory of the University of Liverpool for their help during this project. I greatly appreciated their willingness to help me and their useful advice. I would like to thank the ERASMUS Student Mobility Fund for their contribution in the financial support. It was a valuable experience to do an internship abroad.

1 | Introduction

Nowadays a significant part of our total energy production is provided by wind energy. To satisfy the growing demand of wind energy, more and better wind turbines are required. In order to improve the designs of wind turbines there is a lot of research going on to flow prediction models in this field. As a result of the increasing amount of computational power of the current computer systems, the numerical methods are becoming more and more popular.

In the past there are a lot of methods developed to predict the flow around wind turbine blades. These methods differ from very complex models to relatively simple 2D approaches. The decision for the use of a method depends on many aspects, like for example the accuracy of the model, the required calculation time and the complexity. In wind turbine design it is important to have a clear understanding of the different models and to be able to make justified choices between the different methods. This report provides a comparison between a 2D BEM method, 3D CFD simulations and experimental data in order to give the reader better insight in the different models and the design of wind turbines.

The first chapter of this report explains the mathematical model behind the used CFD-Solver. This chapter is composed of publications from the University of Liverpool about the HMB-Solver [11] [27] [31]. After the introduction of the CFD-solver the Blade Element Momentum method is introduced. Subsequently the 2D and 3D CFD simulations are described after which the results of these simulations will be compared with the results of the BEM based method and the experimental data. In this project the NREL Annex XX blade is used as a reference blade, since there is a lot of experimental data available regarding this blade.

This report is part of a 3 month intern-ship during the final year of a Master degree in Fluid Dynamics at the University of Twente. This intern-ship is performed at the CFD-laboratory of the University of Liverpool under supervision of Dr. R. Steijl, Prof. G.N. Barakos and Prof. H. W. M. Hoeijmakers.

2 | Mathematical Models for Rotor Flow Simulations

This chapter provides a explanation of the CFD solver that is developed by the University of Liverpool and is used in this project for the CFD simulations. This chapter is composed of publications of people connected to the University of Liverpool who developed this solver. This chapter doesn't include work that is performed as part of the internship but has the aim to explain the solver and to provide some extra information for the interpretation of the results. This chapter is based on the material provided by the University of Liverpool and previously published in [19] [27] [37] [9].

2.1 The Helicopter Multi-Block CFD Solver

The flow solver has been revised and updated over a number of years and has been successfully applied to a variety of problems including cavity flows, dynamic stall, rotors, wind turbines and full helicopter configurations amongst others. HMB is a 3D multi-block structured solver for the Navier-Stokes equations in the 3D Cartesian frames of reference. The Navier-Stokes equations consist of Partial Differential Equations (PDEs) describing the laws of conservation for:

- mass (continuity equation),
- momentum (Newton's 2nd Law), and
- energy (1st Law of Thermodynamics).

The continuity equation simply states that the mass must be conserved. In Cartesian coordinates, x_i, this is written as

$$\frac{\partial \rho}{\partial t} + \frac{\partial \left(\rho u_i\right)}{\partial x_i} = 0 \tag{2.1}$$

where ρ is the density of the fluid, t is the time and u_i is the velocity vector. In the above, Einstein's notation is used, which implies summation for repeated indices.

The second conservation principle states that momentum must be conserved. It is written in Cartesian coordinates as

$$\frac{\partial \left(\rho u_i\right)}{\partial t} + \frac{\partial \left(\rho u_i u_j\right)}{\partial x_j} = \rho f_i - \frac{\partial p}{\partial x_i} + \frac{\partial \tau_{ij}}{\partial x_j} \tag{2.2}$$

where f_i represents body forces, p the pressure and τ_{ij} the Newtonian stress tensor, which is defined as

$$\tau_{ij} = \mu \left[\left(\frac{\partial u_i}{\partial x_j} + \frac{\partial u_j}{\partial x_i} \right) - \frac{2}{3} \delta_{ij} \frac{\partial u_k}{\partial x_k} \right] \quad , \tag{2.3}$$

with μ the molecular viscosity and δ_{ij} the Kronecker delta, defined as

$$\delta_{ij} = \begin{cases} 1 & \text{if} \quad \mathrm{i = j} \\ 0 & \text{otherwise} \end{cases} \tag{2.4}$$

The third principle can be written in Cartesian coordinates as

$$\frac{\partial \rho E}{\partial t} + \frac{\partial}{\partial x_j} \left[u_i \left(\rho E + p \right) \right] - \frac{\partial}{\partial x_j} \left(u_i \tau_{ij} - q_j \right) = 0. \tag{2.5}$$

where E is the total energy of the fluid per unit volume, defined as

$$E = \left[e + \frac{1}{2} u_i u_i \right] \tag{2.6}$$

and e is the specific internal energy with $u_i u_i$ representing the kinetic energy.

The heat flux vector, q_i, is calculated using Fourier's Law

$$q_i = -k_T \frac{\partial T}{\partial x_i} \tag{2.7}$$

where k_T is the heat transfer coefficient and T is the temperature of the fluid.

An ideal gas approximation is used, and the adiabatic index is set to $\gamma = 1.4$. Sutherland's law is used to calculate the viscosity:

$$\mu = \mu_{ref} \left(\frac{T}{T_{ref}} \right)^{\frac{3}{2}} \frac{T_{ref} + T_{Suth}}{T + T_{Suth}} \tag{2.8}$$

2.1.1 Vector Form of the Conservation Laws

These three laws of conservation can be combined and written in the equation shown below, which is referred to as the Navier-Stokes equation of viscous flow. For brevity, vector notation is used

$$\frac{\partial \mathbf{W}}{\partial t} + \frac{\partial \left(\mathbf{F}^i + \mathbf{F}^v \right)}{\partial x} + \frac{\partial \left(\mathbf{G}^i + \mathbf{G}^v \right)}{\partial y} + \frac{\partial \left(\mathbf{H}^i + \mathbf{H}^v \right)}{\partial z} = S_{NS} \tag{2.9}$$

where $\mathbf{W}$ is the vector of conserved variables and is defined by

$$\mathbf{W} = \left(\rho, \rho u, \rho v, \rho w, \rho E \right)^T \tag{2.10}$$

with the variables ρ, u, v, w, p and E having their usual meaning of density, the three components of velocity, pressure and total energy, respectively. The superscripts i and v in Equation 2.9 denote the inviscid and viscid components of the flux vectors $\mathbf{F}$ (in the x-direction), $\mathbf{G}$ (in the y-direction) and $\mathbf{H}$ (in the z-direction). The inviscid flux vectors, $\mathbf{F}^i$, $\mathbf{G}^i$ and $\mathbf{H}^i$, are given by

$$\begin{aligned} \mathbf{F}^i &= \left(\rho u, \rho u^2 + p, \rho u v, \rho u w, u \left(\rho E + p \right) \right)^T \quad , \\ \mathbf{G}^i &= \left(\rho v, \rho u v, \rho v^2 + p, \rho v w, v \left(\rho E + p \right) \right)^T \quad , \\ \mathbf{H}^i &= \left(\rho w, \rho u w, \rho v w, \rho w^2 + p, w \left(\rho E + p \right) \right)^T \quad , \end{aligned} \tag{2.11}$$

while the viscous flux vectors, $\mathbf{F}^v$, $\mathbf{G}^v$ and $\mathbf{H}^v$, contain terms for the heat flux and viscous forces exerted on the body and can be represented by

$$\begin{aligned}
\mathbf{F}^v &= \frac{1}{\mathrm{Re}}\left(0, \tau_{xx}, \tau_{xy}, \tau_{xz}, u\tau_{xx} + v\tau_{xy} + w\tau_{xz} + q_x\right)^T \quad , \\
\mathbf{G}^v &= \frac{1}{\mathrm{Re}}\left(0, \tau_{xy}, \tau_{yy}, \tau_{yz}, u\tau_{xy} + v\tau_{yy} + w\tau_{yz} + q_y\right)^T \quad , \\
\mathbf{H}^v &= \frac{1}{\mathrm{Re}}\left(0, \tau_{xz}, \tau_{yz}, \tau_{zz}, u\tau_{xz} + v\tau_{yz} + w\tau_{zz} + q_z\right)^T \quad .
\end{aligned} \tag{2.12}$$

S_{NS} represents source terms. In most calculations, these terms are set to 0, however, for hovering rotors, a fixed grid approach is used and a source term is then added:

$$S_{NS} = [0, -\rho\vec{\omega} \times \vec{u_h}, 0]^T \tag{2.13}$$

where $\vec{u_h}$ is the local velocity field in the rotor-fixed frame of reference.

Although the Navier-Stokes equations completely describe turbulent flows, the large number of temporal and spatial turbulent scales associated with high Reynolds numbers make it difficult to resolve all the turbulent scales computationally[33]. In such circumstances, the number of turbulent scales are reduced by time averaging the Navier-Stokes equations to give the Reynolds-Averaged Navier-Stokes equations (RANS). This results in additional unknowns (called Reynolds stresses) which must be modelled[28]. The fluid stress tensor mentioned in Equation 2.12 is then approximated by the Boussinesq hypothesis[4], more description of which is provided in the following sections.

2.1.2 Numerical Methods

The HMB solver uses a cell-centred finite volume approach combined with an implicit dual-time method. In this manner, the solution marches in pseudo-time for each real time-step to achieve fast convergence. According to the finite volume method, the RANS equations can be discretised for each cell by

$$\frac{d}{dt}\left(\mathbf{W}_{i,j,k}\mathcal{V}_{i,j,k}\right) + \mathbf{R}_{i,j,k} = 0. \tag{2.14}$$

where $\mathcal{V}_{i,j,k}$ denotes the cell volume and $\mathbf{R}_{i,j,k}$ represents the flux residual.

The implicit dual-time method proposed by Jameson[15] is used for time-accurate calculations. The residual is redefined to obtain a steady state equation which can be solved using acceleration techniques. The following system of equations are solved in the implicit scheme during the time integration process

$$\frac{\Delta V\mathbf{W}^{m+1}_{i,j,k} - \Delta V\mathbf{W}^{m}_{i,j,k}}{\Delta V\Delta\tau} + \frac{\Delta V\mathbf{W}^{n+1}_{i,j,k} - \Delta V\mathbf{W}^{n}_{i,j,k}}{\Delta V\Delta t} = \mathbf{R}^{n+1}_{i,j,k} \tag{2.15}$$

where ΔV is the change in cell volume, $\Delta\tau$ is the pseudo time-step increment and Δt is the real time-step increment. The flux residual $\mathbf{R}^{n+1}_{i,j,k}$ is approximately defined by

$$\mathbf{R}^{n+1}_{i,j,k} \approx \mathbf{R}^{n}_{i,j,k} + \frac{\partial\mathbf{R}^{n}_{i,j,k}}{\partial\mathbf{W}^{n}_{i,j,k}}\left(\mathbf{W}^{n+1}_{i,j,k} - \mathbf{W}^{n}_{i,j,k}\right) \tag{2.16}$$

By substituting Equation 2.16 into Equation 2.15, the resulting linear system can be written as

$$\left(\frac{1}{\Delta t} + \left(\frac{\partial\mathbf{R}}{\partial\mathbf{W}}\right)^n\right)\Delta\mathbf{W} = -\mathbf{R}^n \tag{2.17}$$

where the subscripts i, j, k have been dropped for clarity and ΔW is used for $\left(\mathbf{W}_{i,j,k}^{n+1} - \mathbf{W}_{i,j,k}^{n}\right)$.

Osher's upwind scheme [26] is used to resolve the convective fluxes although Roe's flux-splitting scheme [29] is also available. The Monotone Upstream-centred Schemes for Conservation Laws (MUSCL) variable extrapolation method[39] is employed in conjunction to formally provide second-order accuracy. The Van Albada limiter is also applied to remove any spurious oscillations across shock waves. The central differencing spatial discretisation method is used to solve the viscous terms. The non-linear system of equations that is generated as a result of the linearisation is then solved by integration in pseudo-time using a first-order backward difference. A Generalised Conjugate Gradient (GCG)[1] method is then used in conjunction with a Block Incomplete Lower-Upper (BILU)[1] factorisation as a pre-conditioner to solve the linear system of equations, which is obtained from a linearisation in pseudo-time.

The flow solver can be used in serial or parallel mode. To obtain an efficient parallel method based on domain decomposition, different methods are applied to the flow solver [42]. An approximate form of the flux Jacobian resulting from the linearisation in pseudo-time is used which reduces the overall size of the linear system by reducing the number of non-zero entries. Between the blocks of the grid, the BILU factorisation is also decoupled thereby reducing the communication between processors. Each processor is also allocated a vector that contains all the halo cells for all the blocks in the grid. Message Passing Interface (MPI) is used for the communication between the processors in parallel. Most computations undertaken in this work have been performed on the Beowulf Pentium 4 130-processor workstations of the CFD Laboratory at the University of Liverpool. For very large grids, however, calculations were conducted on different supercomputing clusters such as HECToR[38] in Edinburgh, UK, and the necessary porting of the code onto these facilities performed. HECToR is based on the Cray XE6 system and comprises 3712 12-core AMD Opteron 2.1GHz Magny Cours processors in 1856 XE6 compute nodes, delivering a peak-performance of 373 Teraflops.

A number of linear and non-linear statistical turbulence models have been implemented into HMB. The one-equation SA turbulence model[34] to realise the turbulent properties for DES computations, and the DDES approach as well as the SALSA modification of the SA turbulence model were implemented for this project. Options for DES with two-equation Wilcox $k-\omega$[40] and Menter's $k-\omega$ Shear-Stress Transport (SST)[22] turbulence models are also available. All these turbulence models and indeed the simulation techniques are described in greater detail in the following sections.

2.2 General Description of Turbulence and its Modelling

Turbulent flows contain structures which show rapid fluctuations in time and space. A broad range of scales are observed to exist at high Reynolds numbers where turbulence develops as an instability of the laminar flow. Starting with the laminar flow, fluid layers slide smoothly past each other and the molecular viscosity dampens any high-frequency small-scale instability. At high Reynolds number, the flow reaches a periodic state. The character of the flow also changes and becomes more diffusive and dissipative. This flow has increased mixing friction, heat transfer rate and spreading rate. Boundary layers consequently become thicker and less susceptible to separation[6].

The non-linearity of the Navier-Stokes equations leads to various interactions between the turbulent fluctuations of different wavelengths and directions. Wavelengths extend from a maximum comparable to the width of the flow to a minimum fixed by viscous dissipation of energy. A key process that spreads the motion over wide range of wavelengths is called vortex stretching[6]. Turbulent structures in the flow gain energy if the vortex elements are primarily orientated in a direction which allow the mean velocity gradients to stretch them. This mechanism is called production of turbulence. The kinetic energy of the turbulent structures is then convected, diffused and dissipated.

Most of the energy is carried by the large scale structures, the orientation of which is sensitive to the mean flow. The large eddies cascade energy to the smaller ones via stretching. Small eddies have less pronounced preference in their orientation and statistically appear to be isotropic. For the shortest wavelengths, energy is dissipated by viscosity. This description corresponds to what is known as isotropic turbulence. For this flow, the ratio of the largest to smaller scale increases with Reynolds number[6].

If the unsteady Navier-Stokes equations are used to calculate the flow, a vast range of length and time scales would have to be computed. This would require a very fine grid and a very high resolution in time. This approach known as Direct Numerical Simulation of turbulence (DNS) is by today's computing speeds applicable only to flows at very low Reynolds number. One technique called Large-Eddy Simulation explicitly resolves the scales away from the wall and exploits modelling in the near-wall regions. A sub-grid scale (SGS) model is used to model the smaller scales which are assumed to be more isotropic. Although less computationally intensive than DNS, this is still expensive, especially for higher Reynolds number flows.

A turbulence model therefore needs to account for some part of the fluctuating motion in order to keep the computing cost down. The optimum model should therefore be simple to implement, general and derived out of the flow physics. It is equally important that the model is computationally stable and co-ordinate invariant. These statistical turbulence models are applied to a special form of the equations of motion called the Reynolds-Averaged Navier-Stokes (RANS) equations. These are obtained by Reynolds averaging the Navier-Stokes equations.

2.3 Reynolds Averaging

In a turbulent flow, the fields of pressure, velocity, temperature and density vary randomly in time. Reynolds' approach involves separating the flow quantities into stationary and random parts. The quantities are then presented as a sum of the mean flow value and the fluctuating part[6]:

$$\varphi = \overline{\varphi} + \varphi' \tag{2.18}$$

This formulation is then inserted into the conservation equations and a process known as Reynolds averaging is performed. Three averaging methods are possible:

- time averaging,
- spatial averaging,
- ensemble averaging.

2.3.1 Time Averaging

Time averaging is the most common averaging method. It can be used only for statistically stationary turbulent flows, i.e. flows not varying with time on the average. For such flows, the mean flow value is defined as

$$\overline{u_i(x)} = \lim_{T\to\infty} \frac{1}{T_{inte}} \int_i^{i+T_{inte}} u_i(x,t)\,\mathrm{d}t \tag{2.19}$$

In practice, $T_{inte} \to \infty$ means that the integration time T_{inte} needs to be long enough relative to the maximum period of the assumed fluctuations.

2.3.2 Spatial Averaging

Spatial averaging can be applied to homogeneous turbulence, which is a type of turbulent flow that is uniform in all directions, on average. In this case, a parameter is averaged over all the spatial directions by performing a volume integral. The mean flow value is then defined as

$$\overline{u_i(t)} = \lim_{V\to\infty} \frac{1}{V} \int\int\int_V u_i(x,t)\,\mathrm{d}t \tag{2.20}$$

where V represents the volume of the domain.

2.3.3 Ensemble Averaging

The most general type of averaging is called ensemble averaging and is applicable to flows that decay in time, for instance. This method of averaging is similar to time-averaging but rather than dividing by the integration time, T_{inte}, the mean flow value is obtained by taking a sum over all the measurements or samples, N, and is defined by

$$\overline{u_i(x)} = \lim_{N\to\infty} \frac{1}{N} \sum_{n=1}^{N} u_i(x,t) \tag{2.21}$$

For turbulent flows that are both stationary and homogeneous, all the three types of averages mentioned above are assumed to be equal. This assumption is referred to as the ergodic hypothesis[6].

By time-averaging the mass, momentum and energy equations, the Reynolds-Averaged Navier-Stokes (RANS) equations are obtained. The continuity equation remains the same since it is linear with respect to velocity. However, extra terms appear in the momentum and energy equations due to the non-linearity of the convection term. These extra terms are called the Reynolds Stresses, τ_{ij}^R, and are defined in tensor notation as being equivalent to $-\rho\overline{u_i'u_j'}$. The time-averaged momentum equation then takes the form

$$\frac{\partial\left(\rho u_i\right)}{\partial t}+\frac{\partial\left(\rho u_i u_j\right)}{\partial x_i}=\rho f_i-\frac{\partial p}{\partial x_i}+\frac{\partial}{\partial x_j}\left(\tau_{ij}+\tau_{ij}^R\right) \tag{2.22}$$

where the overbar has been dropped from the mean values for clarity. A similar result is obtained for the energy equation (Equation 2.23):

$$\frac{\partial\rho E}{\partial t}+\frac{\partial}{\partial x_j}\left[u_i\left(\rho E+p\right)\right]-\frac{\partial}{\partial x_j}\left(u_i\left(\tau_{ij}+\tau_{ij}^R\right)-q_j^R\right)=0. \tag{2.23}$$

where q_j^R is the turbulent heat flux. The main problem in turbulence modelling involves calculating the Reynolds stresses, from the known mean quantities. One common approach is based on Boussinesq's approximation.

2.4 Boussinesq-Based Models

The Boussinesq approximation is based on an analogy between viscous and Reynolds stresses and expresses the Reynolds stresses as a product of the eddy viscosity (μ_T) and the velocity gradient. Boussinesq's eddy viscosity hypothesis states that

$$-\rho\overline{u_i'u_j'}=\mu_T\left[\left(\frac{\partial u_i}{\partial x_j}+\frac{\partial u_j}{\partial x_i}\right)-\frac{2}{3}\delta_{ij}\frac{\partial u_k}{\partial x_k}\right]-\frac{2}{3}\rho\delta_{ij}k \tag{2.24}$$

where k represents the specific kinetic energy of the fluctuations and is given by

$$k\equiv\frac{u_i'u_i'}{2} \tag{2.25}$$

The key idea behind Boussinesq's hypothesis is that the Reynolds stresses can be calculated as a product of the dynamic eddy-viscosity, μ_T, and the strain-rate tensor of the mean flow, i.e.

$$-\rho\overline{u_i'u_j'}=2\mu_T S_{ij}-\frac{2}{3}\delta_{ij}k \tag{2.26}$$

where

$$S_{ij}=\frac{1}{2}\left(\frac{\partial u_i}{\partial x_j}+\frac{\partial u_j}{\partial x_i}-\frac{2}{3}\delta_{ij}\frac{\partial u_k}{\partial x_k}\right) \tag{2.27}$$

The eddy viscosity, μ_T, is a scalar and consequently the Reynolds stress components are linearly proportional to the mean strain-rate tensor. What is also implied here is that compressibility plays a secondary rate in the development of the turbulent flow-field. According to Morkovin's hypothesis [24], compressibility affects turbulence only at hypersonic speeds.

To compute μ_T, further modelling is required and it is at this point that turbulence models come into play. Turbulence models are classified into categories based on the number of transport equations required to calculate μ_T. According to the number of transport equations needed for the calculation of the eddy viscosity, the Boussinesq-based models are classified as:

- algebraic or zero-equation models, such as the Cebeci-Smith[5] and Baldwin-Lomax[2] models,
- one-equation models, such as the Spalart-Allmaras (SA)[34] and Baldwin-Barth (BB)[3] models.

- two-equation models, such as the $k-\omega$[40], $k-\varepsilon$[17], $k-\omega$ baseline (BSL) and shear-stress transport (SST)[22] and $k-g$[23] models.
- multi-equation models: three-equation[12, 10, 8], four-equation[32], five-equation [21] and multiple time-scale [13, 18, 7] models.

An additional family of models solves equations for all components of the Reynolds stress tensor. These are also known as Reynolds Stress Models (RSM), second-order closures or second-moment closures.

2.5 Viscosity-Dependent Parameters

Non-dimensionalised wall distances for turbulent flow, y^*, and non-turbulent flow, y^+, are defined by the following

$$y^* \equiv \frac{y_n k^{1/2}}{\nu}, \qquad y^+ \equiv \frac{y_n u_\tau}{\nu}, \tag{2.28}$$

where y_n is the distance from the nearest wall, $u_\tau \equiv \sqrt{\tau_w/\rho}$ is the friction velocity and τ_w represents the dynamic wall shear stress. Turbulent Reynolds numbers for the $k-\varepsilon$ model (denoted by R_t) and for the $k-\omega$ model (denoted by R_ω) are given by the following equation

$$R_t \equiv \frac{k^2}{\nu\varepsilon}, \qquad R_\omega \equiv \frac{k}{\nu\omega} \quad , \tag{2.29}$$

which represents the importance of the eddy over molecular viscosity.

2.6 Two-Equation Models

By far the most popular type of turbulence model used is of the two-equation type. Two-equation models are ‘complete’, i.e. can be used to predict properties of a given flow with no prior knowledge of the turbulence structure or flow geometry. Two transport equations are used for the calculation of the turbulent kinetic energy, k, and turbulence length scale, l, or a function of it. The choice of the 2nd variable is arbitrary and many proposals have been presented. The most popular involves using:

- ε — specific dissipation rate of turbulence.
- ω — k-specific dissipation rate.
- τ — turbulent time-scale.

A description of the different types of two-equation models is provided in Table 2.1 below. As well as indicating the variable used for the second transport equation, Table 2.1 includes the equation used to calculate the eddy viscosity.

One of the most widely used two-equation turbulence models is the $k-\varepsilon$ model. One of the original versions of this model was developed by Jones and Launder [17] in 1972. The turbulent scale in the $k-\varepsilon$ model is calculated using a second transport equation for the turbulent dissipation rate, ε. The eddy viscosity for the $k-\varepsilon$ model is typically derived from

$$\mu_T = C_\mu \rho \frac{k^2}{\varepsilon} \tag{2.30}$$

Table 2.1: Different types of two-equation turbulence models and the corresponding second variable.

Two-Equation Model	Equation	2nd Variable Used
Kolmogorov (c. 1942) [20]	$k^{1/2}l^{-1}$	ω (Frequency Length Scale)
Rotta (c. 1950)	l	
Harlow-Nakayama (1967) [14]	$k^{3/2}l^{-1}$	ε (Energy Dissipation Rate)
Spalding (1969) [35]	kl^{-2}	ω'^2 (Vorticity fluctuations squared)
Speziale (1992) [36]	$lk^{-1/2}$	τ (Time-Scale)
Nee	kl	kl (k times length scale)
Harlow-Nakayama	$lk^{-1/2}$	ν_t (Eddy viscosity)

where C_μ is the model coefficient. The advantage of the $k-\varepsilon$ model is that it performs well for attached flows with thin shear layers and jets but fails to predict the correct flow behaviour in many flows with adverse pressure gradients, extended separated flow regions, swirl, buoyancy, curvature secondary flows and unsteady flows.

The other class of two-equation turbulence models that is widely used is the $k-\omega$ model. In 1988, Wilcox[40] developed the famous $k-\omega$ model originally conceived by Kolmogorov. The $k-\omega$ model is similar to the $k-\varepsilon$ model but instead uses the k-specific dissipation rate as a second variable to compute the turbulent length scale. The eddy viscosity is obtained by

$$\mu_T = \rho\frac{k}{\omega} \tag{2.31}$$

Although the $k-\omega$ model provides better performance in adverse pressure gradient flows, it suffers largely from the same problems as the $k-\varepsilon$ model. Hybrid versions of the $k-\omega$ and $k-\varepsilon$ models called the $k-\omega$ baseline (BSL) and $k-\omega$ shear-stress transport (SST) models were later introduced by Menter[22]. These, in particular the $k-\omega$ SST version, perform well in separated flows. The idea behind the $k-\omega$ BSL model is to exploit the robust and accurate formulation of the $k-\omega$ model near the wall but to also take advantage of the lack of sensitivity to free-stream values of the $k-\varepsilon$ model away from the wall. Menter[22] achieved this by transforming the $k-\varepsilon$ model into the same format as the $k-\omega$ formulation. This process generated an additional cross-diffusion parameter in the ω transport equation. For the SST model[22], the idea was to improve the $k-\omega$ BSL model by including terms to account for the transport of the principal shear stress. This term is incorporated in Reynolds Stress Models (RSM) and was also applied in the Johnson-King model[16]. Its importance was realised based on the significantly improved results for adverse pressure gradient flows[22].

2.6.1 Model Equations: Linear $k-\omega$ Model

Mathematical formulations of the different types of the linear $k-\omega$ two-equation turbulence models discussed in the previous sections are described here. More information on the $k-\varepsilon$ and $k-g$ models can be obtained from [25].

Since the introduction of the linear $k-\omega$ model by Wilcox in 1988[40], the other notable modification to the $k-\omega$ model came from Menter in 1994[22] who proposed the hybridisation of the $k-\omega$ model with the $k-\varepsilon$ model, as described previously. Table 2.2 lists the four notable versions of the $k-\omega$ models and further describes if they include parameters to compute the low Reynolds number properties.

Table 2.2: Different types of linear $k-\omega$ turbulence models

Type of Model	**Low-Re**
Wilcox (1988)[40]	Yes
Wilcox (1994)[41]	Yes
Menter (1994)[22] — (i) BSL Model	Yes
Menter (1994)[22] — (ii) SST Model	Yes

Turbulence transport equations used in the formulation of the $k-\omega$ models are given by the following:

$$\frac{\partial}{\partial t}(\rho k)+\frac{\partial}{\partial x_j}(\rho U_j k)=\frac{\partial}{\partial x_j}\left[\left(\mu+\frac{\mu_T}{\sigma_k}\right)\frac{\partial k}{\partial x_j}\right]+\rho\left(P_k-\beta^*\omega k\right) \tag{2.32}$$

$$\frac{\partial}{\partial t}(\rho\omega)+\frac{\partial}{\partial x_j}(\rho U_j\omega)=\frac{\partial}{\partial x_j}\left[\left(\mu+\frac{\mu_T}{\sigma_\omega}\right)\frac{\partial\omega}{\partial x_j}\right]+\rho\left(\frac{\alpha}{\nu_t}P_\omega-\frac{\beta}{\beta^*\omega^2}\right)+\rho S_l \tag{2.33}$$

In the transport equation for k and ω above, the production of turbulence, P, and the dissipation rate specific to k, P_ω, is defined by

$$P_k=\tau_{ij}^R\frac{\partial u_i}{\partial x_j},\qquad P_\omega=\rho\frac{\alpha}{\nu_t}P_k. \tag{2.34}$$

Values for the coefficients used in all the four types of linear $k-\omega$ models discussed here are given in the Table 2.3.

Menter's models[22] are constructed as a 'blend' of the $k-\omega$ and $k-\varepsilon$ models. Here the $k-\varepsilon$ model is phrased in the same form as the $k-\omega$ model so as to exploit its independence of free-stream values. Blending of the $k-\varepsilon$ and $k-\omega$ model values for α, β, σ_k^{-1} and σ_ω^{-1} is (in this notation) given by the following equation

$$B\begin{pmatrix} a \\ b \end{pmatrix}\equiv F_1 a+(1-F_1)\,b. \tag{2.35}$$

The blending function is defined by

$$F_1=\tanh\left(\mathrm{arg}_1^4\right), \tag{2.36}$$

where

$$arg_1=\min\left[\max\left(\frac{k^{1/2}}{\beta^*\omega y},\frac{500\nu}{y_n^2\omega}\right),\frac{2k\omega}{y_n^2\max\left(\nabla k\cdot\nabla\omega,0.0\right)}\right]. \tag{2.37}$$

The $k-\omega$ SST model places an additional vorticity-dependent limiter on the shear-stress

$$F_2=\tanh\left(arg_2^2\right),\qquad arg_2=\max\left(\frac{2k^{1/2}}{\beta^*\omega y},\frac{500\nu}{y^2\omega}\right). \tag{2.38}$$

Table 2.3: Values of constants used in linear $k-\omega$ models.

Type of Model	α^*	β^*	α	β
Wilcox (1988)[40]	1	$\frac{9}{100}$	$\frac{5}{9}$	$\frac{3}{40}$
Wilcox (1994)[41]	$\frac{\frac{1}{40}+\frac{R_\omega}{6}}{1+\frac{R_\omega}{6}}$	$\frac{9}{100}\frac{\frac{5}{18}+\left(\frac{R_\omega}{8}\right)^4}{1+\left(\frac{R_\omega}{8}\right)^4}$	$\frac{5}{9}\frac{\frac{1}{10}+\frac{R_\omega}{2.7}}{1+\frac{R_\omega}{2.7}}$	$\frac{3}{40}$
Menter (1994)[22] *(BSL)* ^{1}	1	0.09	$B\begin{pmatrix} 0.553 \\ 0.440 \end{pmatrix}$	$B\begin{pmatrix} 0.075 \\ 0.083 \end{pmatrix}$
Menter (1994)[22] *(SST)* ^{2}	$\min\left(1, \frac{0.31}{F_2}\frac{\omega}{\overline{w}}\right)$	0.09	$B\begin{pmatrix} 0.553 \\ 0.440 \end{pmatrix}$	$B\begin{pmatrix} 0.075 \\ 0.083 \end{pmatrix}$

Type of Model	$\sigma_{\mathbf{k}}$	σ_ω	$\mathbf{S_l}$
Wilcox (1988)[40]	2	2	0
Wilcox (1994)[41]	2	2	0
Menter (1994)[22]*(BSL)* ^{1}	$\frac{1}{B\begin{pmatrix} 0.5 \\ 1.0 \end{pmatrix}}$	$\frac{1}{B\begin{pmatrix} 0.5 \\ 0.856 \end{pmatrix}}$	$B\begin{pmatrix} 0 \\ \frac{1.71}{\omega}\nabla k\cdot\nabla\omega \end{pmatrix}$
Menter (1994)[22]*(SST)* ^{2}	$\frac{1}{B\begin{pmatrix} 0.85 \\ 1.0 \end{pmatrix}}$	$\frac{1}{B\begin{pmatrix} 0.5 \\ 0.856 \end{pmatrix}}$	$B\begin{pmatrix} 0 \\ \frac{1.71}{\omega}\nabla k\cdot\nabla\omega \end{pmatrix}$

Note that this model also uses a slightly different value of σ_k.

For low-Reynolds number versions of the $k-\omega$ model and Menter's $k-\omega$ BSL and SST models, the following boundary conditions are assumed for a direct integration to the wall

$$\text{For } k\text{:} \quad k_w = 0, \qquad flux(k)_w = 0 \quad , \tag{2.39}$$

$$\text{For } \omega\text{:} \quad \omega = 0, \qquad flux(\omega)_w = -\nu\nabla\omega \quad . \tag{2.40}$$

where the subscript w denotes the value *at* the wall.

3 | BEM Method

For the Blade Element Momentum theory (BEM) there is a combination used of the momentum theory, which was developed by Glauert (for propellers) and Betz (for windmills), and the blade element theory. The momentum theory refers to a control volume analysis for the conservation of momentum while the blade element theory refers to a force analysis of a blade section as function of the incoming flow and the blade geometry. In the BEM theory the forces of the blade element method are related to the change in momentum of the momentum theory. This makes it possible to do calculations about the performance characteristics per annular section of the rotor.

3.1 Momentum Theory

Since a wind turbine extract energy from the flow, the energy of the flow is decreasing and the real velocity of the flow around the blades is lower than the free-stream velocity. In the momentum theory the velocities are corrected by the introduction of induction factors. The axial momentum theory enables to derive a relation between the axial force and the axial induction factor while the tangential momentum theory results in a relation between the in plane forces and the angular induction factor.

3.1.1 Axial Momentum Theory

The axial momentum theory applies the conservation laws on a 1D stream tube. The rotor of the wind turbine is considered as a uniform actuator disc that introduces a pressure discontinuity. The reason that an actuator disc is considered as a rotor with a infinite number of blades is that a uniform flow is assumed, which is not possible with a finite number of blades.The situation can be sketched as presented in Figure 3.1.

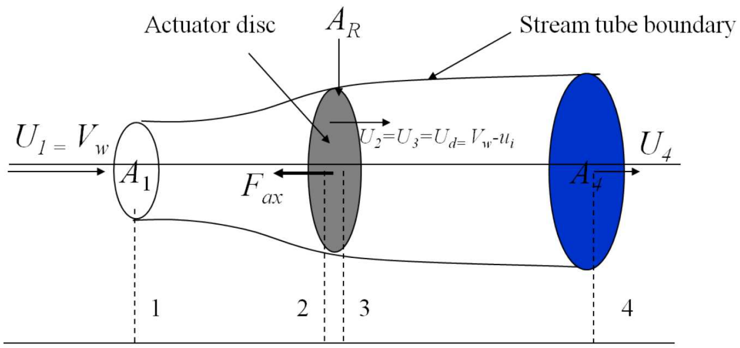

Figure 3.1: Stream tube with indicated the velocities [30]

The axial momentum theory is valid for the following assumptions:

- Steady, incompressible and 1D flow
- Uniform homogeneous and non turbulent flow
- No frictional drag
- No heat transfer
- The rotor disc can be considered as a rotor with an infinite number of blades

Applying the conservation laws to the stream tube sketched in Figure 3.1 results in the following equations from respectively the conservation of mass, momentum and energy.

$$\dot{m} = \rho U_1 A_1 = \rho U_d A_d = \rho U_4 A_4 \tag{3.1}$$

$$T = \dot{m}(U_4 - U_1) \tag{3.2}$$

$$P_{ow} = T U_d = \frac{1}{2}\dot{m}(U_1^2 - U_4^2) \tag{3.3}$$

Where $\dot{m}$ is the mass flux [kg/s], ρ the density in $[\mathrm{kg/m^3}]$, P_{ow} the power extracted by the actuator disc [W], T the thrust force in axial direction in [N], A_1, A_4, A_d the sectional surface area's of the stream tube in $[\mathrm{m^2}]$ as displayed in Figure 3.1 and U_1, U_4, U_d the velocities indicated in Figure 3.1 in [m/s]. Combining equation 3.2 and 3.3 leads to a relation for the velocity U_d at the disc:

$$U_d = \frac{P_{ow}}{T} = \frac{\frac{1}{2}\dot{m}(U_1^2 - U_4^2)}{\dot{m}(U_4 - U_1)} = \frac{1}{2}(U_1 + U_4) \tag{3.4}$$

Defining the axial induction factor as the fractional decrease of the wind velocity at the rotor plane with respect to the free stream wind velocity:

$$a = \frac{U_\infty - U_d}{U_\infty} \tag{3.5}$$

Where U_∞ is the free stream velocity which is equal to the velocity U_1 in Figure 3.1. Rewriting this will result in an expression for the velocity at the rotor plane as a function of the induction factor.

$$U_d = U_\infty(1-a) \tag{3.6}$$

Substituting equation 3.6 into equation 3.4 leads to an expression for the downstream velocity U_4.

$$U_4 = U_\infty(1-2a) \tag{3.7}$$

Since U_1 and U_4 can both be described by a function of U_∞ and a the axial thrust can be expressed as a function of these variables, by using equation 3.2

$$T = \dot{m}(U_4 - U_1) = \rho U_\infty^2 2a(1-a)A_r \tag{3.8}$$

with A_r the surface area of the rotor plane. In order to express the axial thrust force as a function of the radius the rotor surface can be divided into annular rings as is shown in Figure 3.2, where dF_{ax} represents the thrust and V_w the free stream velocity. The axial thrust force for each ring can than be determined by:

$$dT(r) = \rho U_\infty^2 4a(1-a)\pi r dr \tag{3.9}$$

Where the surface area of the annular ring is determined by $A_r = 2\pi r dr$.

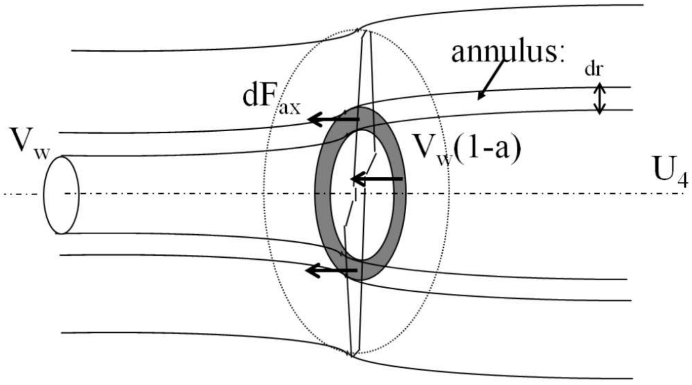

Figure 3.2: Division in annular rings [30]

3.1.2 Tangential Momentum Theory

The tangential momentum theory enables to find a relation between the torque of the rotor and an angular induction factor. The concept for this theory is shown in Figure 3.3 where position 2 is just upstream of the disc, position 3 just downstream of the disc and d indicates the position of the disc itself.

Applying the conservation law for angular momentum to an infinitesimal ring of the rotor disc as sketched in Figure 3.3 leads to the following expression:

$$dQ(r) = \dot{m}r(\omega_1 r - \omega_4 r) \tag{3.10}$$

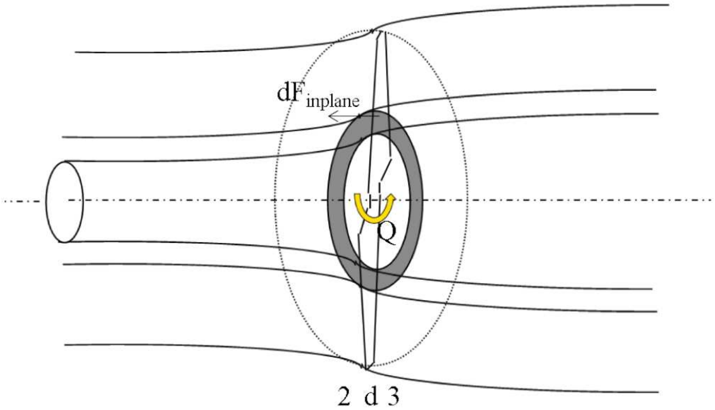

Figure 3.3: Tangential momentum concept for in plane forces [30]

Where dQ is defined as the torque in the rotor plane, $\dot{m}$ the mass flow through the rotor plane, $\omega_1 r$ and $\omega_4 r$ respectively the rotational velocity of the upstream and the downstream flow and r as the radius of the annular ring. Since is assumed that the upstream flow is uniform and not rotating, ω_1 can be set to zero. Defining ω_4 as the wake rotation cause by the torque and using equation 3.1 and 3.6 in combination with equation 3.10 leads to the next equation:

$$dQ(r) = \rho U_\infty 2(1-a)r^3\omega_4 \pi dr \tag{3.11}$$

Where for the surface area an infinitesimal ring of the cross section is taken and where ω_4 the wake rotation is defined in [rad/s]. In a similar way as is done for the axial momentum theory can be proved that the wake rotation at the rotor disc can be written as a function of the rotational velocity and the angular induction factor [30]:

$$\omega_d = \frac{1}{2}\omega_4 = a'\Omega \tag{3.12}$$

Substituting this in equation 3.11 leads to the following equation for the torque:

$$dQ(r) = \rho U_\infty 4a'(1-a)r^3\Omega \pi dr \tag{3.13}$$

3.1.3 Blade Element Theory

The blade element theory evaluate the aerodynamic forces on each section of the blade as a function of the geometric properties and the inflow angle. When the inflow angle is calculated the aerodynamic forces can be obtained from corresponding data of the airfoil section. The Blade Element Momentum theory is based on the following assumptions:

- The flow is steady, incompressible and 2D
- The flow is uniform, homogeneous and non turbulent

- There is no aerodynamic interaction between the elements (so no flow in radial direction)
- The forces of the blades are only determined by lift and drag characteristics
- Free-stream flow is perpendicular to the plane of rotation (so no yaw)
- The blades are assumed to be rigid

For each section along the radius the angles and velocities can be defined as shown in Figure 3.4. The geometric angle is defined as the pitch angle increased by the local twist angle of the section. The difference between this angle and the relative inflow angle can be defined as the local angle of incidence:

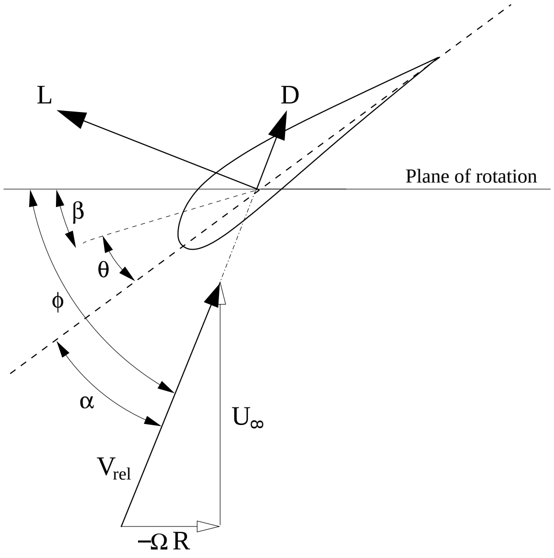

Figure 3.4: Definition of the different angles

$$\alpha = \phi - (\theta + \beta) \tag{3.14}$$

where α is the sectional angle of incidence [deg], θ the geometric twist angle [deg] and β the pitch angle of the blade [deg].

When considering the aerodynamic forces with the blade element theory and the aid of Figure 3.4, the next equations can be derived:

$$dT(r) = B\frac{1}{2}\rho U_{rel}^2 \left(C_l \cos(\phi) + C_d \sin(\phi)\right) cdr \tag{3.15}$$

$$dQ(r) = B\frac{1}{2}\rho U_{rel}^2 \left(C_l \sin(\phi) - C_d \cos(\phi)\right) crdr \tag{3.16}$$

where dT is the contribution to the thrust in [N] per section dr, dQ the contribution to the torque in [Nm], B the number of blades, ϕ the relative inflow angle [deg], U_{rel} the relative velocity in [m/s], ρ density in $[\mathrm{kg/m^3}]$, C_l the lift coefficient [-], C_d the drag coefficient [-], c the chord of the local section in [m] and r the radial position of the section in [m]. The relative velocity in the above equations depends on the induced axial and rotational velocity. With the aid of Figure 3.4 and the use of the induced velocities the relative velocity and the relative inflow angle can be defined by the following equations:

$$\begin{aligned} U_{rel} &= \sqrt{\left(U_\infty\left(1-a\right)\right)^2 + \left(\Omega r\left(1+a'\right)\right)^2} && (3.17) \\ \phi &= \arctan\left(\frac{U_\infty\left(1-a\right)}{\Omega r\left(1+a'\right)}\right) && (3.18) \end{aligned}$$

where the relative velocity U_{rel} is defined in [m/s], U_∞ represent the free stream wind velocity in [m/s], a the axial induction factor [-], ϕ the relative inflow angle in [deg], a' the angular induction factor [-], Ω the rotational velocity in [rad/s] and r the radial position at the blade in [m]. Since above equations are dependent on the radius r the relative velocity and inflow angle differs for every section. Using equation 3.18 and the definition of the speed ratio makes it possible to derive an equation for the relation between the two induction factors:

$$\begin{aligned} \tan(\phi) &= \frac{1-a}{\lambda_r\left(1+a'\right)} \\ a &= 1-\tan(\phi)\lambda_r\left(1+a'\right) && (3.19) \end{aligned}$$

where λ_r is defined as the speed ratio [-]:

$$\lambda_r = \frac{\Omega r}{U_\infty} \qquad (3.20)$$

3.2 BEM Model

Coupling the momentum theory with the blade element theory will result in the BEM model. This is accomplished by coupling the relations for the thrust and the torque from both methods. So equating and rewriting equations 3.9, 3.13, 3.15 and 3.16 results in the following expressions:

$$
\begin{aligned}
U_\infty^2 4a(1-a)\pi r &= Bc\frac{1}{2}U_{rel}^2(C_l\cos(\phi)+C_d\sin(\phi)) \qquad (3.21)\\
4a'(1-a)U_\infty\pi r^2\Omega &= Bc\frac{1}{2}U_{rel}^2\left(C_l\sin(\phi)-C_d\cos(\phi)\right) \qquad (3.22)
\end{aligned}
$$

The definitions for the relative velocity, introduced in equation 3.17 and 3.18, can be combined to:

$$
U_{rel}=\frac{U_\infty\left(1-a\right)}{\sin(\phi)} \qquad (3.23)
$$

Substituting this in equation 3.21 and 3.22 and rewrite this equations will lead to an expression for the axial and angular induction factors:

$$
\begin{aligned}
8a\pi r\sin(\phi)^2 &= Bc\left(1-a\right)\left(C_l\cos(\phi)+C_d\sin(\phi)\right)\\
\frac{a}{(1-a)} &= \frac{Bc\left(C_l\cos(\phi)+C_d\sin(\phi)\right)}{8\pi r\sin(\phi)^2} \qquad (3.24)
\end{aligned}
$$

Where in the equation for the angular induction factor, equation 3.19 is substituted for the axial induction factor a in order to obtain an equation for a' independent of a:

$$
\begin{aligned}
8a'\pi r^2\Omega\sin(\phi)^2 &= BcU_\infty\left(1-a\right)\left(C_l\sin(\phi)-C_d\cos(\phi)\right)\\
\frac{a'}{(1-a)} &= \frac{BcU_\infty\left(C_l\sin(\phi)-C_d\cos(\phi)\right)}{8\pi r^2\Omega\sin(\phi)^2}\\
\frac{a'}{1-\left(1-\tan(\phi)\lambda_r\left(1+a'\right)\right)} &= \frac{Bc\left(C_l\sin(\phi)-C_d\cos(\phi)\right)}{8\pi r\lambda_r\sin(\phi)^2}\\
\frac{a'}{(1+a')} &= \frac{Bc\left(C_l\sin(\phi)-C_d\cos(\phi)\right)}{4\pi r\sin(2\phi)} \qquad (3.25)
\end{aligned}
$$

For a given wind velocity, blade geometry and operating conditions, the problem can be described by equation 3.18, 3.14, 3.24 and 3.25, which are repeated below. When the aerodynamic data of the used profiles is available these equations can be solved in an iterative way. After doing a first guess for the induction factors, these equations can be solved and will result in a 'new' value for the induction coefficients. This process can be repeated until the difference in the induction factors reaches an acceptable limit. Repeating this for every section dr along the radius leads to a solution for the whole blade.

$$\begin{aligned}\phi &= \arctan\left(\frac{1-a}{\lambda_r\,(1+a')}\right)\\ \alpha &= \phi-(\theta+\beta)\\ \frac{a}{(1-a)} &= \frac{Bc\,(C_l(\alpha)\cos(\phi)+C_d(\alpha)\sin(\phi))}{8\pi r\sin(\phi)^2}\\ \frac{a'}{(1+a')} &= \frac{Bc\,(C_l(\alpha)\sin(\phi)-C_d(\alpha)\cos(\phi))}{4\pi r\sin(2\phi)}\end{aligned}$$

For the above set of equations the influence of the wind velocity and the operating conditions is captured in the speed ratio λ_r which can be calculated using equation 3.20. When these equations are solved other properties like the thrust, torque, induced velocity and the local lift coefficient can be determined. This can be done with either the equations derived from the momentum theory or the equation from the blade element theory. To calculate the torque and the thrust per section dr the following equations are used:

$$dT(r) = \rho U_\infty^2 4a(r)\,(1-a(r))\,\pi r dr \tag{3.26}$$

$$dQ(r) = 4a'(r)\,(1-a(r))\,\rho U_\infty \pi r^3\Omega dr \tag{3.27}$$

By summing all the sectional values for the thrust and the torque the total thrust and torque per blade can be obtained.

$$T = \sum_{r_0}^{R}\frac{dT(r)}{B} \tag{3.28}$$

$$Q = \sum_{r_0}^{R}\frac{dQ(r)}{B} \tag{3.29}$$

In order to check this model the calculations for the thrust and the torque can be repeated with the equations derived from the blade element method:

$$dT_{BE}(r) = B\frac{1}{2}\rho U_{rel}^2\,(C_l(r)\cos(\phi(r))+C_d(r)\sin(\phi(r)))\,cdr \tag{3.30}$$

$$dQ_{BE}(r) = B\frac{1}{2}\rho U_{rel}^2\,(C_l(r)\sin(\phi(r))-C_d(r)\cos(\phi(r)))\,crdr \tag{3.31}$$

The performance of a wind turbine is often expressed in terms of power. To eliminate the direct influence of the wind speed, the dimensionless power coefficient is computed, which is the ratio between the extracted power and the power available in the flow. The power coefficient can be defined as:

$$C_{pow} = \frac{P_{ow}}{\frac{1}{2}\rho U_\infty^3 A} \tag{3.32}$$

where P is the power extracted by the wind turbine in [W] defined as $P = T\Omega$, A the surface area of the rotation plane of the blades in [m^2] and U_∞ the free stream wind velocity in [m/s]. To see what the contribution of each section dr is to the total power coefficient the sectional power coefficient can be computed by:

$$\begin{aligned} C_{pow}(r) &= \frac{\Omega 4a'(r)\left(1-a(r)\right)\rho U_{\infty}\pi r^{3}\Omega dr}{\frac{1}{2}\rho U_{\infty}^{3}2\pi r dr} \\ &= \lambda_r^2 4a'(r)\left(1-a(r)\right) \qquad (3.33) \end{aligned}$$

where equation 3.9 is substituted for the torque, $2\pi r dr$ is substituted for A, since this is the surface area of the annular rings and the velocity ratio is replaced by λ_r^2. Equation 3.33 suggests that a higher speed ratio and a low axial induction factor should result in a higher power coefficient. But since the speed ratio and the induction factors are related to each other is it difficult to see directly how the power coefficient will behave by varying this parameters. But as is known from the theory of Betz, the maximum power is produced for an axial induction factor of 0.333.

4 | 2D-CFD

In this project 2 dimensional and 3 dimensional CFD simulations are performed. The results of the 2D simulations are used in combination with the Blade Element Momentum model for a 2D model for the prediction of the performance of wind turbine blades. Since the S809 profile is the only geometry which is used for the blades in this project, the simulations that will be discussed are limited to this airfoil section only.

4.1 The Grid

In CFD simulations the grid forms an important factor in obtaining reliable results. In order to have more control over the grid, a structured grid is build. The advantages of a structured grid are that the size and the shape can be controlled better than for unstructured grids. For example in the area close to the surface a very fine grid is desired, while in the area further away from the surface a coarser grid will satisfy. Also the junction between these two area's need to be designed carefully since adjacent cells can't vary to much for a good solution. Apart from the size also the shape can be controlled better with structured grids. For reliable results the corners of all the cells need to approach the 90 degrees as close as possible. These conditions need to be observed more severe in area's where the flow properties have big gradients, then in area's where the changes are small as in the far field for example. Since the S809 airfoil section has a sharp trailing edge the grid is based on the so called C-topology. In order to predict the flow in the boundary layer a very fine grid is required around the

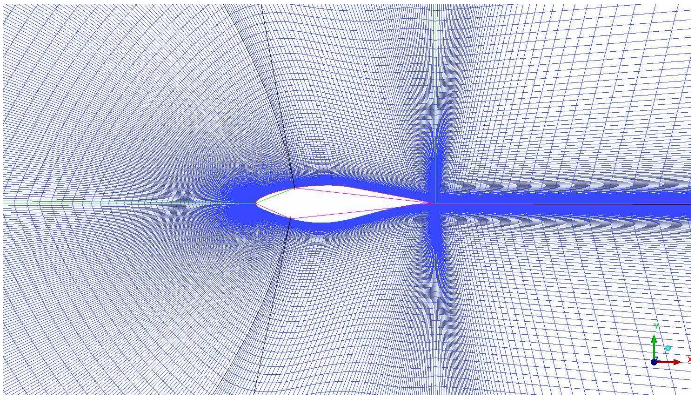

Figure 4.1: 2D grid of the S809 airfoil section

surfaces. For an estimation of the size of these cells the inverse Reynolds number is calculated:

$$h \approx \frac{1}{Re} = \frac{\mu}{\rho v L}$$

where h represents the dimensionless height of the cells at the surface [-], μ the dynamic viscosity of the medium [Pa.s], ρ the density in $[\mathrm{kg/m^3}]$, v the velocity in [m/s] and L a characteristic length in [m], which is in this case the chord of the airfoil (1 m). From this equation follows that the size of the cells at the surface need to be in the order of 10^{-5}. Since in the area where the flow separates from the surface also a finer grid is desired there is also a clustering introduced around the trailing edge as can be seen in Figure 4.1. The size of the cells around the trailing edge starts at 10^{-4} and grows exponentially. The grid that is used for the simulations contains 94.680 cells and is displayed in Figure 4.1.

4.2 Results 2D-CFD

The aim of the 2D-CFD simulations is to obtain aerodynamic data about the used airfoil sections for the BEM model. For the grid described above steady simulations are performed for different angles of incidence. The angles of incidence that are evaluated are the angles between -8 and 20 degrees. This captures the whole domain of interest for applications in wind energy. The simulations are done with two turbulence models, the $k-\omega$ and the $k-\omega-SST$ model. The differences between these methods are discussed in section 4.2.2. After running the simulations for all the different angles the results can be collected and the graphs in Figure 4.2 can be drawn. In Figure 4.2 can be seen that flow separation starts to occur around an 12 degrees angle of incidence. In Figure 4.2 the contributions of the pressure and friction forces on the drag coefficient are shown. This are the values obtained by the integration of respectively the pressure and the friction coefficient which are described by:

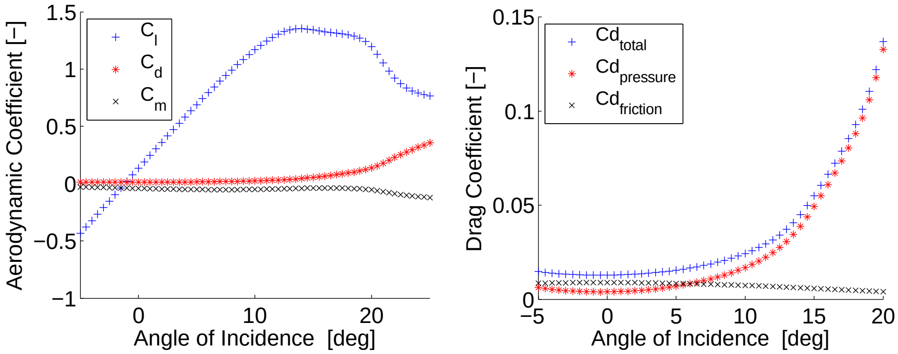

(a) Aerodynamic coefficients

(b) Friction and pressure drag

Figure 4.2: Aerodynamic properties of the S809 airfoil section, obtained by the 2D-CFD simulations

$$C_p = \frac{P - P_\infty}{\frac{1}{2}\rho U_\infty^2} \quad \text{and} \quad C_f = \frac{\tau_w}{\frac{1}{2}\rho U_\infty^2} \tag{4.1}$$

where τ_w is the wall shear stress in $[N/m^2]$. There can be noticed that the contribution to the drag by the friction terms is more or less constant and independent of the angle of incidence, while the contribution of the pressure terms increase substantially by increasing the angle of incidence. For the lower angles of attack the friction part has a dominant contribution to the total drag while for angles bigger than 5 degrees the pressure part takes the main share. Figure 4.3 on page 28 shows the results of the CFD simulations.

In Figure 4.3a the pressure is displayed in terms of the pressure coefficient. In Figure 4.3b there is zoomed in on the leading edge of the profile to show the changes in the C_p and the stagnation point which can be recognised by the dark red spot. Figure 4.3c till 4.3e presents the transition from fully attached flow to flow separation. The last figure, Figure 4.3f shows the velocity close to the surface. In this figure the boundary layer with the no slip condition at the wall can be noticed.

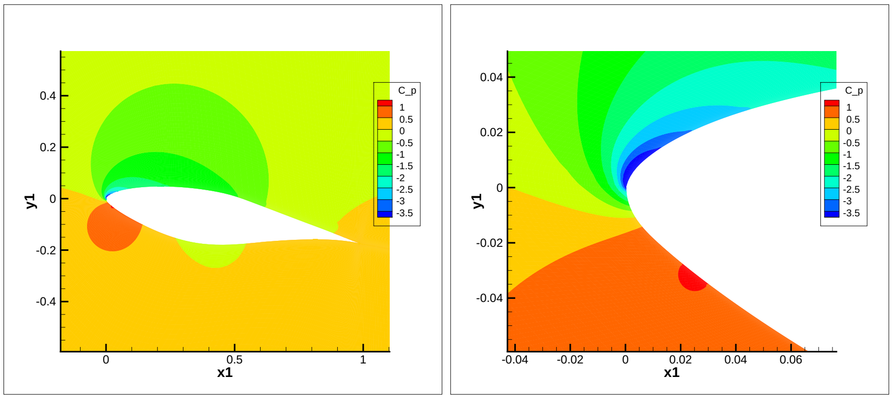

(a) Pressure coefficient for an angle of attack of 10 degrees

(b) Pressure coefficient at the nose of the profile for an angle of attack of 10 degrees

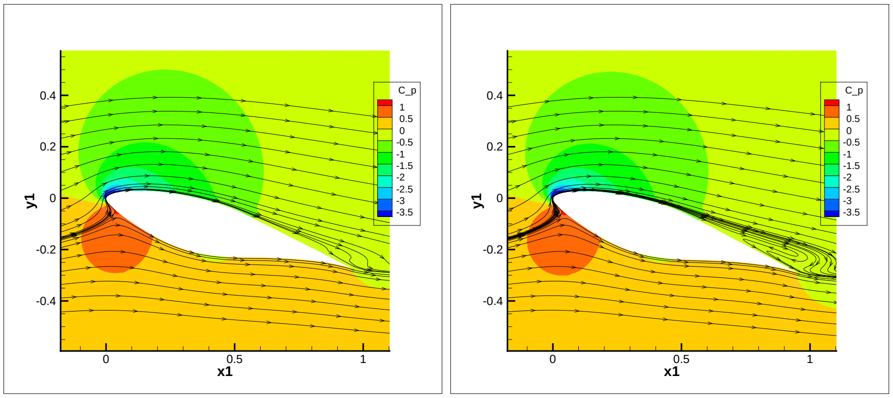

(c) Streamlines for an angle of attack of 16 degrees

(d) Streamlines for an angle of attack of 16 degrees

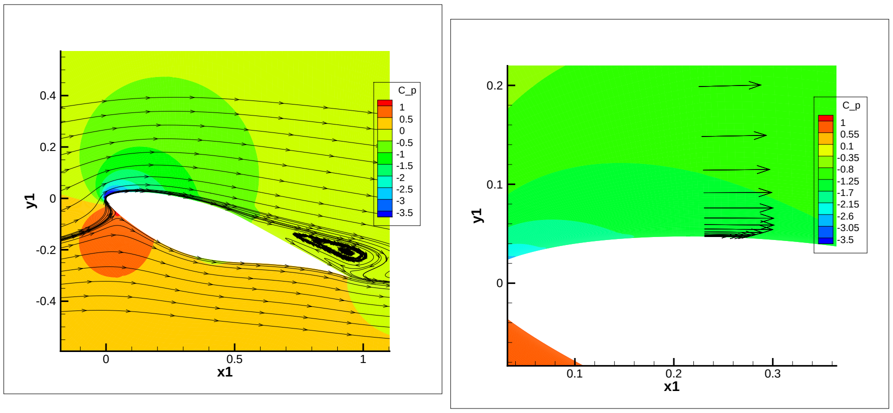

(e) Streamlines for an angle of attack of 18 degrees

(f) Velocity in the boundary layer

Figure 4.3: Visualisation of the flow around the 2D airfoil

4.2.1 Convergence of the solution

In order to be able to judge about the reliability of the results first a convergence check is performed. The HMB solver provides a few ways to check this convergence. One way is to look at the values of the C_l, C_d and C_m, and look what the changes are. If at a certain point the changes are nearly zero it can be concluded that the values are converged. In Figure 4.4 the values of C_l, C_d and C_m are plotted as function of the number of iterations. Keep in mind that a converged solution not directly means that the solution is the correct answer to the problem since the quality of the grid plays an important role in the accuracy and reliability of the solution. In Figure 4.4 and 4.5 the convergence of the C_l, C_d and C_m values are shown for an angle of incidence of 5 degrees and a Reynolds number of 2.000.000. This convergence behaviour is representative for all the 2D simulations that are carried out during this project.

The plots in Figure 4.4 show the convergence of the pressure terms as a function of the number of iterations. It can be seen that the values are scattered in the beginning but start to converge after about 1500 iterations. In Figure 4.4c the moment coefficient around the leading edge is shown instead of the moment coefficient around the quarter chord. In the results this is converted to a quarter chord coefficient. The same check is performed for the friction terms of the coefficients and is shown in Figure 4.5.

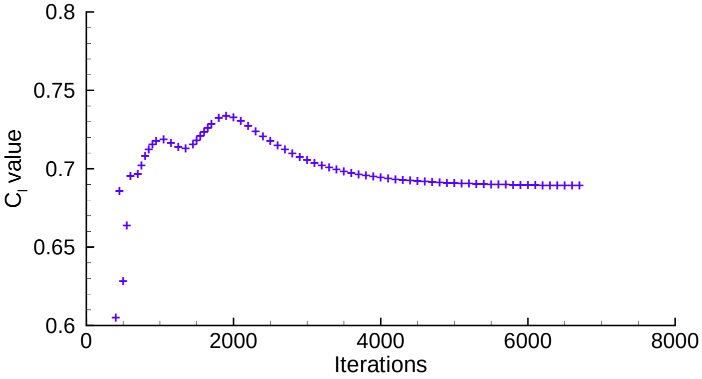

(a) The convergence of the pressure terms of the C_l, for an angle of incidence of 5 deg

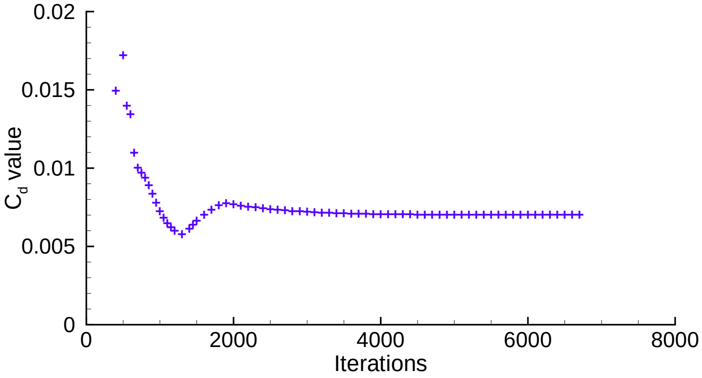

(b) The convergence of the pressure terms of the C_d, for an angle of incidence of 5 deg

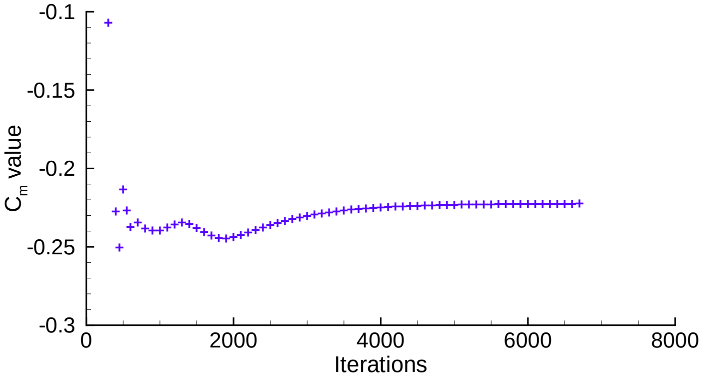

(c) The convergence of the pressure terms of the C_m, for an angle of incidence of 5 deg

Figure 4.4: The convergence of the pressure terms of the coefficients

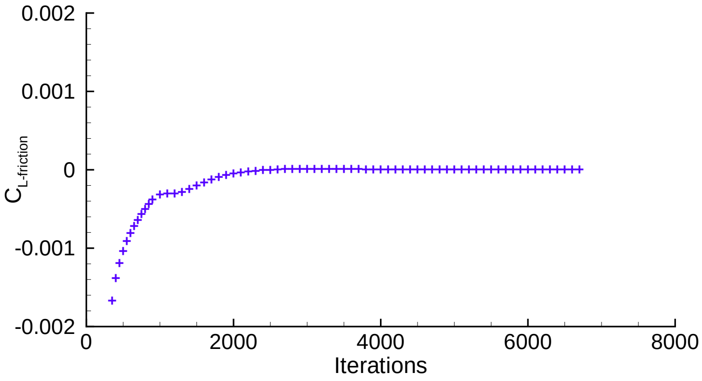

(a) The convergence of the friction terms of the C_l, for an angle of incidence of 5 deg

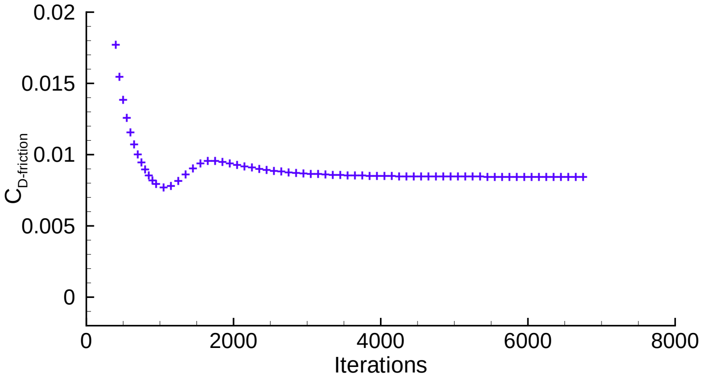

(b) The convergence of the friction terms of the C_d, for an angle of incidence of 5 deg

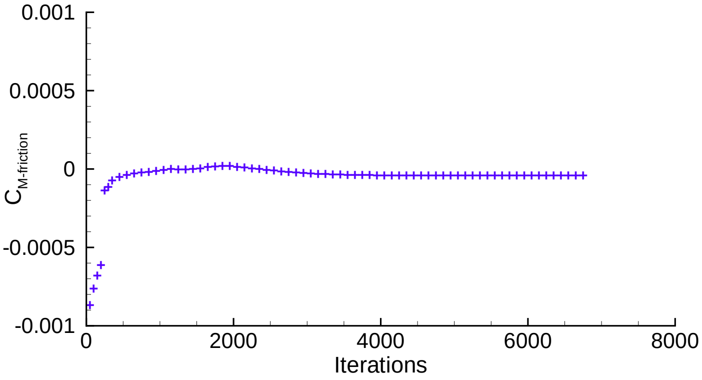

(c) The convergence of the friction terms of the C_m, for an angle of incidence of 5 deg

Figure 4.5: The convergence of the friction terms of the coefficients

A second way to check the convergence is to look at the residual. In this case the residual is checked with the L2 norm which is defined as:

$$L2\_RES = \sqrt{\frac{\sum\limits_{i=1}^{N} \sum\limits_{m=1}^{M} (RES_{i,j})^2}{M * N}} \tag{4.2}$$

where i is the index of the grid point, N the total number of points in the grid, m the index of the element in RES and M the total number elements in RES. The value of the L2 norm is the residual averaged over the different cells and variables and is often plotted on a logarithmic scale. In the HMB solver the L2 norm is expressed as the logarithm of the ratio between the initial residual and the current residual.

$$\log_{10}\left(\frac{L2\_RES}{L2\_RES_{initial}}\right) \tag{4.3}$$

In the figure below this logarithmic L2 norm is plotted versus the number of iteration steps for the simulation with a 5 degrees angle of incidence. Also the residual of the turbulence model for this case is displayed in the figure below.

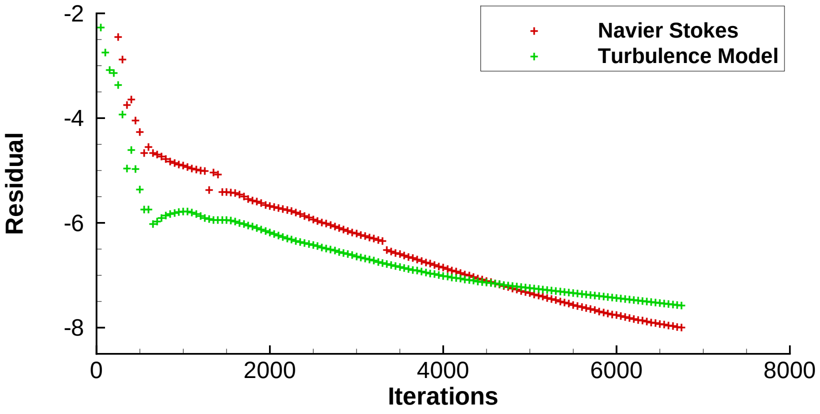

Figure 4.6: Logarithm of the residual of the Navier-Stokes equations

4.2.2 Turbulence modelling

Since CFD simulations are very sensible for differences in the simulation parameters and the choice of the turbulence model, these simulations are carried out with two different turbulence models. The $k-\omega$ and the $k-\omega-SST$ model. The former model is a 2 transport equation model developed by Wilcox in 1988 [40] that solves equations for the kinetic energy k and the turbulence frequency ω. The $k-\omega-SST$ model is an extension of the $k-\omega$ model and includes an extra term which accounts for the transport effect of turbulent shear stress. The $k-\omega-SST$ uses a blending function between the $k-\omega$ model which is applied in the area close to the wall and the standard $k-\epsilon$ model which is used further away from the wall. The advantage of the $k-\omega-SST$ model is that it predicts the point of separations a bit later because this model is less sensitive for the inlet turbulence.

To get an impression of the influence of the different turbulence models the C_l and C_d values of both models are compared in Figure 4.7. There can be seen that the behaviour is similar for both models except for the area where separation occurs. The $k-\omega-SST$ model tends to predict the flow separation a bit later.

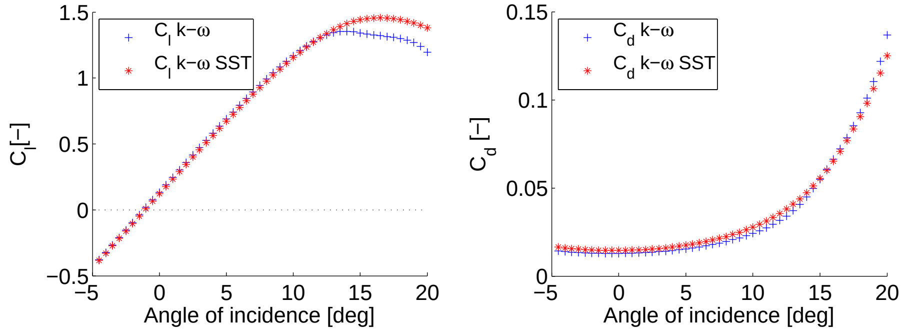

(a) Lift coefficient

(b) Drag coefficient

Figure 4.7: The influence of the different turbulence models on the lift and drag coefficient

5 | 3D-CFD

For the 3 dimensional simulation there is a grid build for the Annex XX blade. This blade is discussed in detail in section 5.1. For this 3D simulations only the $k-\omega-SST$ model is applied.

5.1 Annex XX blade

The blade that is analysed in this project is the NREL Annex XX blade. The Annex XX is a full scale wind turbine with a diameter of 10 m for which a lot of experiments are performed. The experiment was conducted in the 24.4x36.6m NASA-Ames wind tunnel, and included mainly pressure measurements. In this project the results of these measurements are compared with the results of the different prediction methods. The Annex XX blade is a blade that is designed with the S809 profile only. The shape of the blade is characterised by the chord and twist distribution which are shown in Figure 5.1:

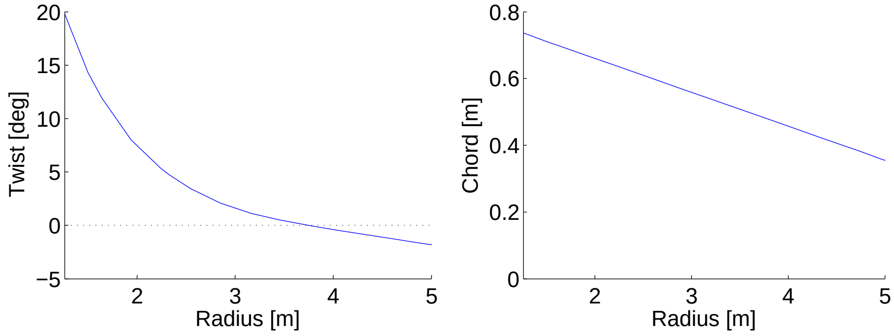

(a) Twist distribution (b) Chord distribution

Figure 5.1: Geometric properties of the Annex XX blade

5.2 The Grid

The topology of the 3D grid is displayed in Figure 5.2. As can be seen in this Figure only one half of the flow domain is modelled in the grid. This is done because the wind turbine has 2 identical blades and the symmetry can be used to reduce the size of the grid. The grid contains 2.495.272 cells which are a lot smaller at the surface, where the flow behaviour in the boundary layer need to be computed.

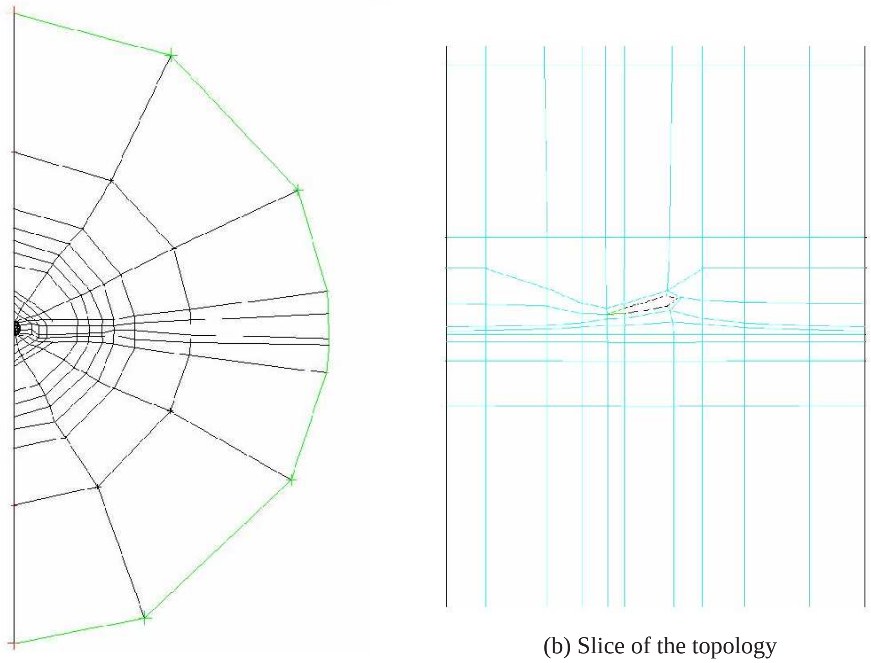

(b) Slice of the topology

(a) Top view of the topology

Figure 5.2: Topology of the 3D grid

Also at the trailing edge the size of the cells are smaller since the changes are expected to be stronger in this area. The cells at the surface and the trailing edge have a dimensionless size of 10^{-5} and grow exponentially. In Figure 5.3 and 5.4 the grid at the blade surface is shown even as a slice of the grid around the blade.

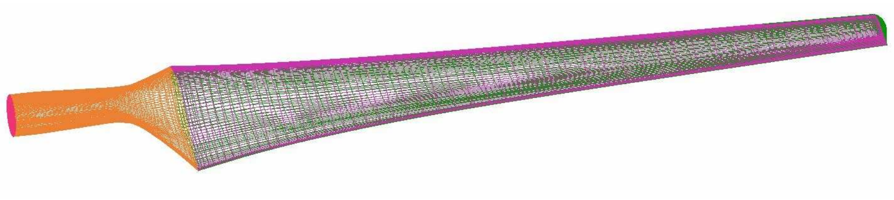

Figure 5.3: The cells of the grid at the surface of the blade

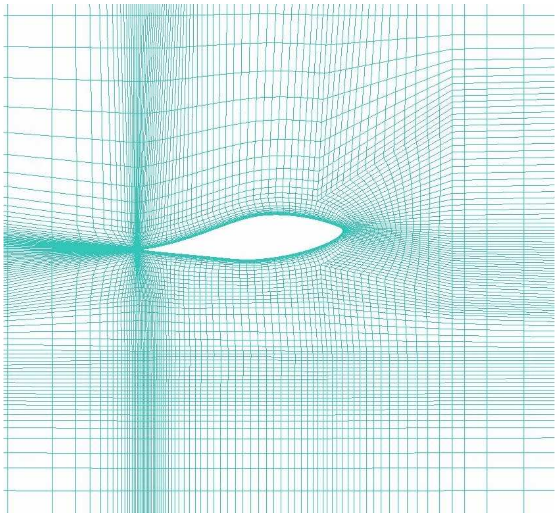

Figure 5.4: A slice of the grid zoomed in on the airfoil section

5.3 3D-CFD Results

The grid described above contains about 2.500.000 cells and is used for the visualisation of the flow around the blade. In Figure 5.5 the streamlines around the blade are shown. The streamlines around the tip and the root of the blade demonstrate the effect of a finite 3D wing. There can be seen that the flow in the mid section of the blade is not influenced by 3D effects of the root and the tip of the blade. The vortices at the root and the tip causes the streamlines at the upper surface to bend towards this outer parts of the blade. As can be seen in Figure 5.5 this effect becomes stronger when approaching the tip or root. For the comparison of the 3D CFD results with the BEM results and the experimental data, the results of a former project are used. Since this was a more advanced model that includes more details about for example the influence of the tower. This grid contains about 18.000.000 cells instead of the 2.500.000 of the grid described above.

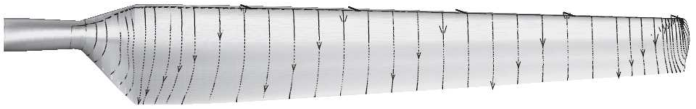

Figure 5.5: The streamlines at the upper surface obtained by 3D simulations

6 | BEM Results and Comparison with 3D CFD

This chapter provides the results of the BEM model which is introduced in chapter 3 and a comparison of this model to the 3D CFD results and experimental data. The blade that is used for this comparison is the NREL Annex XX blade which is described in section 5.1.

6.1 Results BEM

Before starting with the comparison between the BEM method, the 3D CFD and the experimental results, first the results of the BEM model are discussed. In the BEM method the sectional data is obtained by CFD simulations with the $k - \omega$ turbulence model. These models are build with Matlab as explained in the preceding chapters. The conditions that are applied to the BEM model are:

- Wind velocity U_∞ of 7 m/s
- Rotational speed Ω of 72 rpm
- Number of blades B is 2
- Pitch angle β is 3 deg (at the tip)
- Whole blade has the S809 profile
- Aerodynamic data is produced by 2D CFD simulation
- Density ρ is equal to 1.20 kg/m^3
- Blade radius of 5 m
- Twist and chord distribution is as shown in Figure 5.1 of section 5.1.

As mentioned before, the system of equations (shown on page 22), needs to be solved in an iterative way. The convergence of the axial induction factor a during this iterations is shown in Figure 6.2 for the first section at the root. This figure is representative for the convergence of the other sections and the angular induction factor as well. The solution of the induction factors is shown in Figure 6.1 where the red line indicates the Betz limit which is the theoretical upper limit for maximum power.

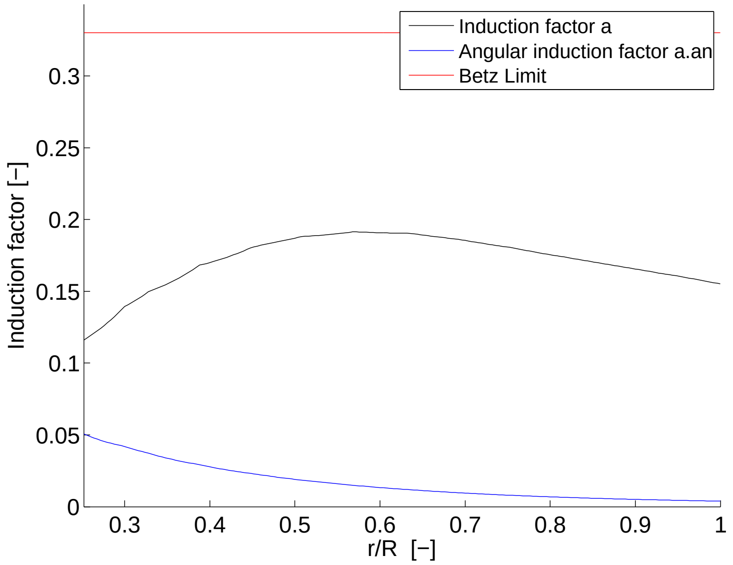

Figure 6.1: The induction factors compared to the Betz limit

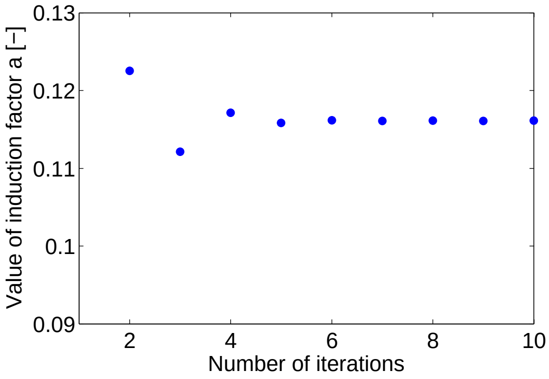

Figure 6.2: The convergence of induction factor a at r = 1.25 m

In Figure 6.3 the geometric twist angle is compared with the different inflow angles. From this figure the effect of induction can be seen by comparing the undisturbed inflow angle with the induced inflow angle. For this conditions the inflow angle will be more or less reduced by 4° which is around 11 percent. The fact that the line of the geometric angle is more or less parallel to the induced inflow angle results in a nearly constant angle of incidence. This explains directly the purpose of twist, since the twist enables the blade to operate at the optimal angle of incidence at every section. In Figure 6.4 can be seen that the sectional lift coefficient C_l is more or less constant along the radius, and is a result of the nearly constant angle of incidence. Since only the component of the force in the plane of rotation can contribute to the torque and the energy production, it is interesting to see what the ratio is between the thrust and torque. This is visualised in Figure 6.4 by adding the components of the C_l and the C_d in thrust and torque direction.

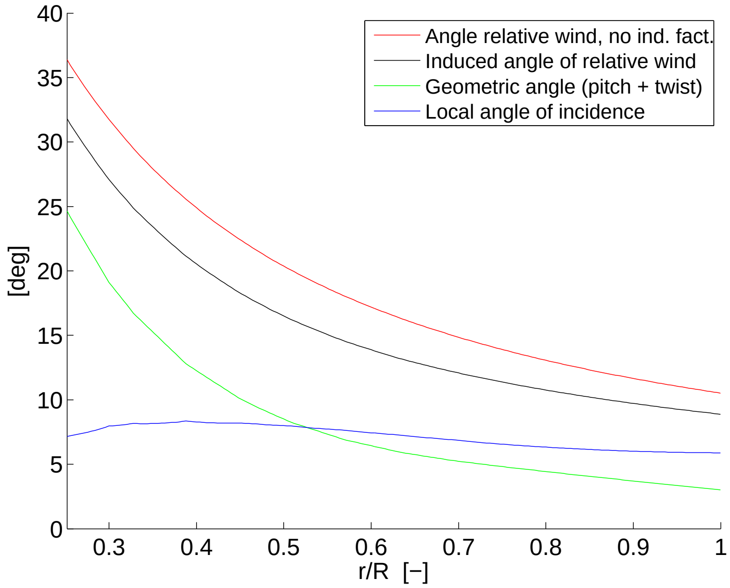

Figure 6.3: The geometric angles compared with the different definition of the inflow angles

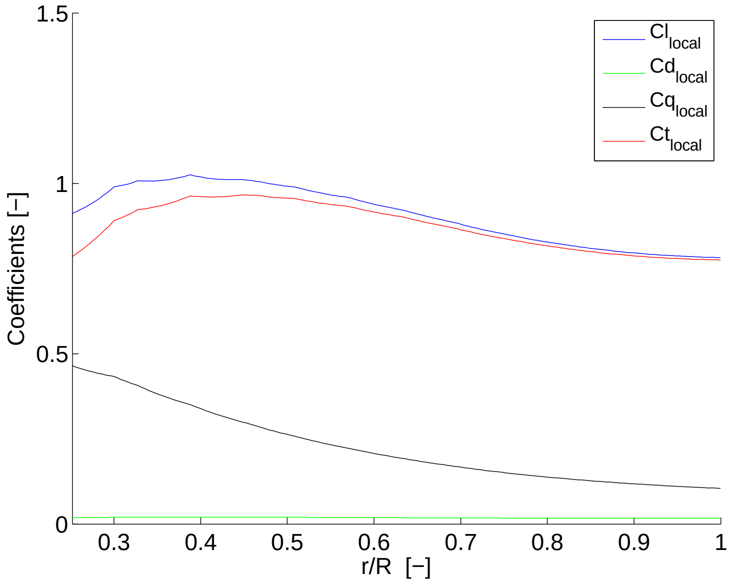

Figure 6.4: The sectional C_l and the components in thrust and torque direction

The actual torque and thrust is calculated with equation 3.27 and 3.29 and is shown in Figure 6.5. In order to get an idea what the forces on the blade are, also the local lift distribution is calculated. There can be seen that the force in torque direction is nearly constant while the thrust and the lift are increasing. This behaviour can be explained by the fact that the direction of these forces is dependent of the relative inflow angle which

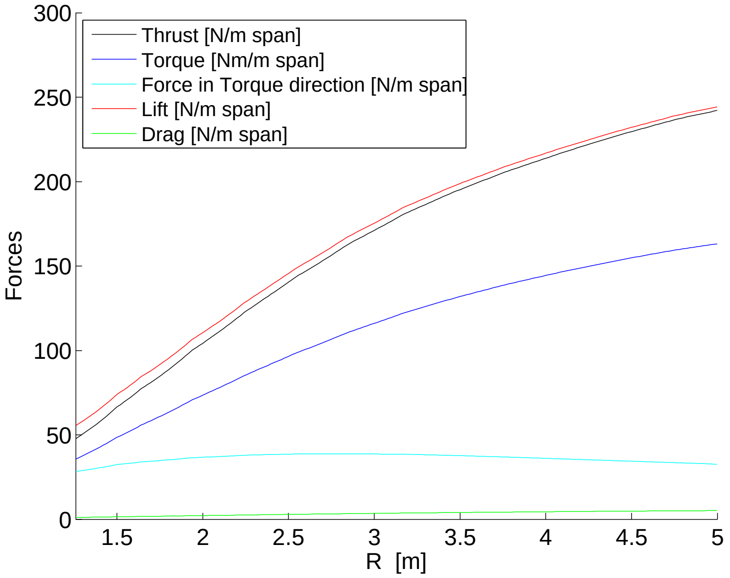

Figure 6.5: The forces and torque along the radius

varies along the radius (see Figure 6.3). So the effects of decreasing chord, decreasing angle of incidence but increasing velocity will in this case result in a constant force in torque direction. The fact that the thrust is almost the same as the lift is caused by the case that the relative inflow angles are very small.

To evaluate the performance of a wind turbine the generated power is an important indicator, which is represented by the power coefficient introduced in section 3.2 on page 22. In Figure 6.6 can be seen that the middle part of the blade has the highest power coefficient for the applied operation conditions. This high power coefficient does not directly mean that the middle section delivers also the biggest contribution to the total power of the wind turbine. The power coefficient shown in Figure 6.6 can be treated as a mark for the efficiency. The fact that the curve decreases to the tip means not directly that the power decreases but that the ratio between produced power and available power gets lower by approaching the tip. This is caused by the fact that the outer circles have a bigger surface area and thus contain more wind power. The overall power coefficient is displayed in Table 6.1 even as the total thrust, torque and power which are obtained by integrating the distributions shown in Figure 6.5. For the overall power coefficient the surface area of the whole disc is taken to determine the wind power, so this includes also the part around the hub.

Torque	$726\,\mathrm{Nm}$
Thrust	$1133\,\mathrm{N}$
Power	$5474\,\mathrm{W}$
Power Coefficient	0.338

Table 6.1: BEM results for $U_\infty = 7$ m/s and $\Omega = 72$ rpm

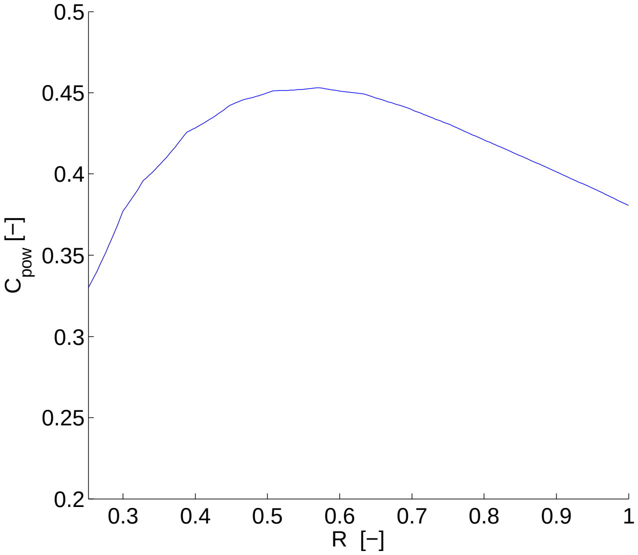

Figure 6.6: The sectional power coefficient C_{pow}

6.2 Comparison

The results of the different methods presented before are compared in this section. Besides a global comparison of the performance parameters like thrust and torque, there is also a more detailed comparison made with sectional data. The methods that are discussed are:

- BEM, 2D-CFD simulations with the $k - \omega$ turbulence model
- 3D CFD simulations with a $k - \omega - SST$ turbulence model and a grid of 18.000.000 cells
- Experimental results obtained from the Annex XX experiment in the NASA-Ames wind tunnel

First the performance in terms of thrust and torque is calculated and compared. The thrust and torque of the experimental results are obtained by integrating the results of the pressure measurement. For the 3D-CFD these values are determined in a similar way by extracting the sections and integrate the pressure around the surface. The procedure for the 2D-CFD BEM methods is described in section 3.2. For the simulations that are used in this 2D model the influence of the friction effects are removed from the data in order to make a fair comparison with the integrated values of the experimental (pressure) data. In Figure 6.7 there can be seen that the thrust and the torque are over estimated by the 2D-CFD method. The suspicion is raised that this is caused by the fact that for the 2D BEM method the 3D flow effects are not taken into account.

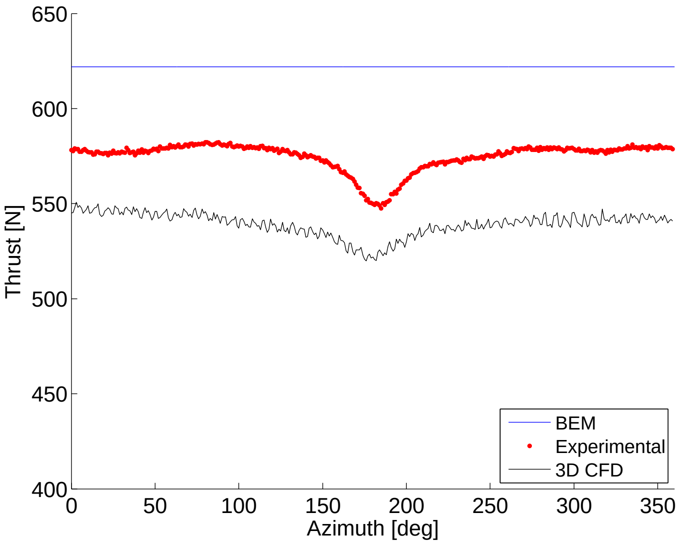

Figure 6.7: The thrust per blade with the tower shadow model

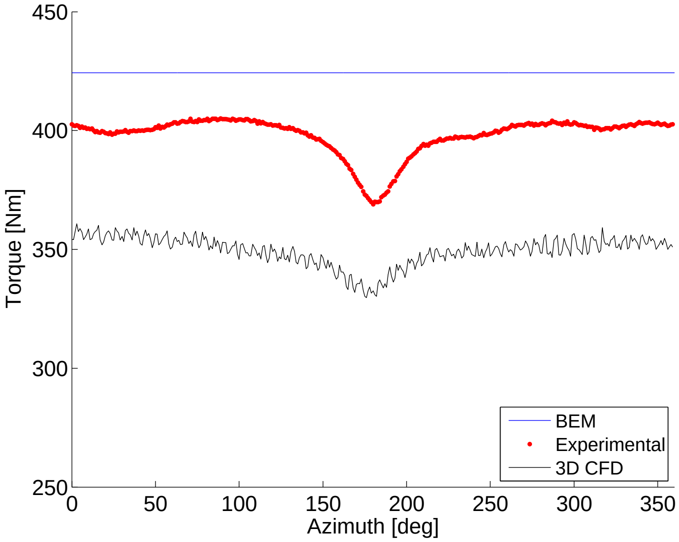

Figure 6.8: The torque with including the tower shadow effects

6.3 Comparison by pressure integration

To get a better idea of what is going on and to investigate the differences in the above results in more detail, the analyse is extended with a comparison of the pressure distributions for different sections along the radius. The pressure is compared for the same sections as where the measurements of the experiments are taken, namely 30, 46, 63, 80 and 95 percent of the radius.

In Figure 6.9 there can be seen that for the section in the middle of the blade the pressure coefficients of the different methods match well. In the area around the root and the tip, arises an over estimation by the 2D methods. This is cause by the fact that losses by 3D effect are not captured in this methods.

To see what the influence of the pressure differences is on the torque and thrust of the wind turbine these C_p plots are integrated. Since for the experimental data there is only a limited amount of measurement points available, it is not possible to get a full description of the C_p curve. To make a fair comparison with the other results the C_p curves of the CFD methods are integrated in the same way. This means that for the CFD methods only the values at the points of the measurements are taken into account, which are pointed out in Figure 6.9. By numerical integration, shown in Figure 6.9, the

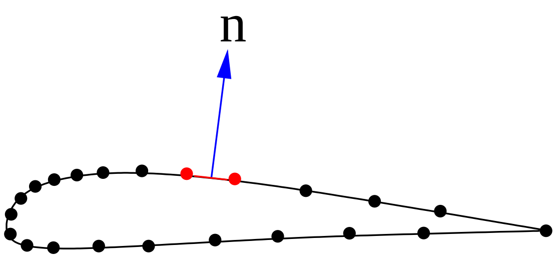

Figure 6.9: Integration of the pressure coefficient

normal, axial and moment coefficient can be calculated:

$$
\begin{aligned}
C_N &= \frac{1}{c}\sum_{i=1}^{n} -C_p(i)n_y(i)ds(i) && (6.1)\\
C_A &= \frac{1}{c}\sum_{i=1}^{n} -C_p(i)n_x(i)ds(i) && (6.2)\\
C_M &= \frac{1}{c^2}\sum_{i=1}^{n} y(i)\left(-C_p(i)n_x(i)ds(i)\right) + x(i)\left(-C_p(i)n_x(i)ds(i)\right) && (6.3)
\end{aligned}
$$

where ds is the length of an infinitesimal part of the contour [m], $C_p(i)$ is the average of the pressure coefficient defined at the end points of ds, C_N is the normal coefficient defined positive pointed upward, C_A is the axial coefficient positive in backward direction and C_M is the moment coefficient defined positive for clockwise rotation. The normal vector $\vec{n}$ in this equations is defined as:

$$\vec{n}(i) = \begin{bmatrix} n_x(i) \\ n_y(i) \end{bmatrix} = \begin{bmatrix} -\frac{dy(i)}{ds(i)} \\ \frac{dx(i)}{ds(i)} \end{bmatrix} \tag{6.4}$$

The results of this integration will be discussed in the next section together with a sensitivity analysis of these values.

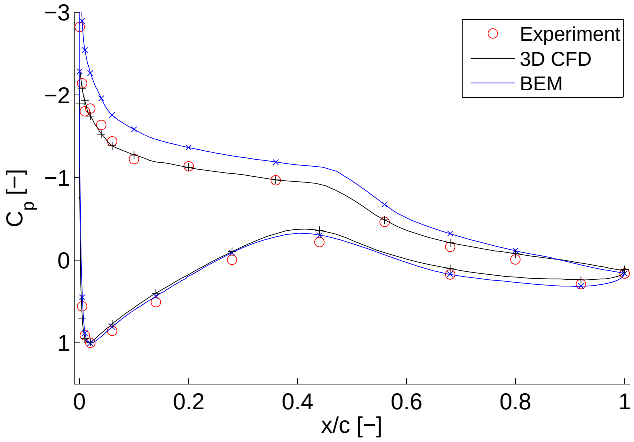

(a) C_p slice at 30%

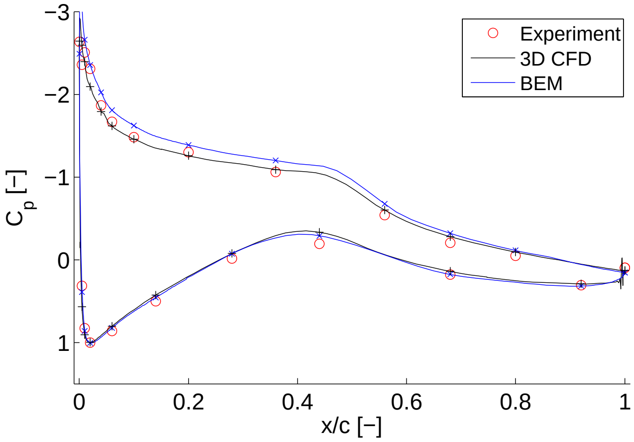

(b) C_p slice at 46%

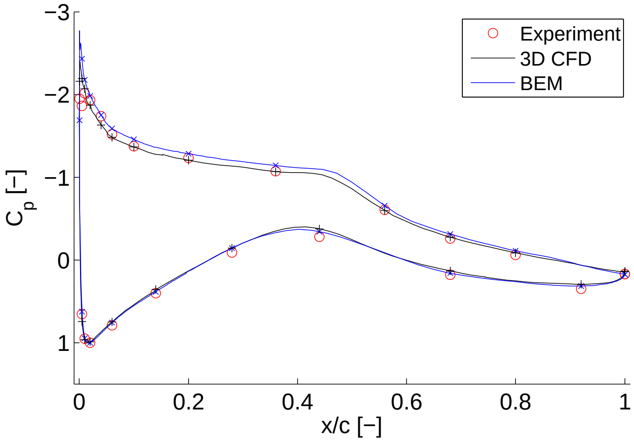

(c) C_p slice at 63%

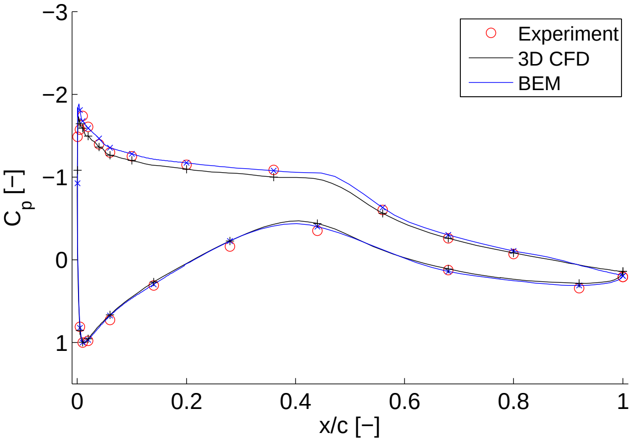

(a) C_p slice at 80%

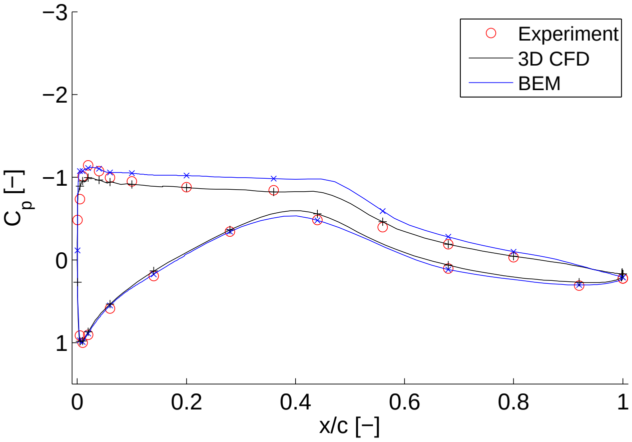

(b) C_p slice at 95%

Figure 6.9: Comparison of the sectional C_p curves

6.3.1 Sensitivity Analysis

For the experimental results there is only data available at the points where the pressure tabs were located. In the comparison above the CFD data is discretized to make a fair comparison. This is done by extracting the values of the CFD data at the same points as were the pressure tabs were located. Subsequently these datasets are integrated in the same way as shown in Figure 6.9. To see what the effect is of this approach a sensitivity analysis is conducted. Imagine for example that the location of the pressure tabs is given within a certain tolerance. What is then the effect of little inaccuracies in the data? This effect is investigated by comparing the difference in the pressure obtained by the CFD simulations in the case the value of the x-coordinate varies within a given tolerance. For example take the point 0.3. If the tolerance is 0.001 the maximum and minimum value of the pressure of the CFD results in the range between 2.999 and 3.001 are compared. When this is repeated for all the points of the experimental data, every point has a maximum and a minimum value for the pressure. To find for example the upper bound of the lift, all the minimum values of the upper surface and all the maximum values for the lower surface are used for the integration. Doing this the other way around will result in a lower bound. Applying this concept to all the coefficients enables to show a range for the deviation as an effect of variations and inaccuracies in the x-coordinate. The results for a tolerance of 1 mm are displayed in Figure 6.9. There can be seen that the normal coefficient is the least sensitive. The axial coefficient is a bit more sensitive and the moment coefficient shows the widest bounds which means that it is the most sensitive one. From Figure 6.9 it can be concluded that the applied method is very sensitive for inaccuracies. To see what the effect is on the torque and thrust coefficient this procedure is repeated and shown below. In Figure 6.9 can be seen that the results of the pressure integration of the moment coefficient differs a lot between the different methods. The cause of this variation is treated in more detail in Appendix A.

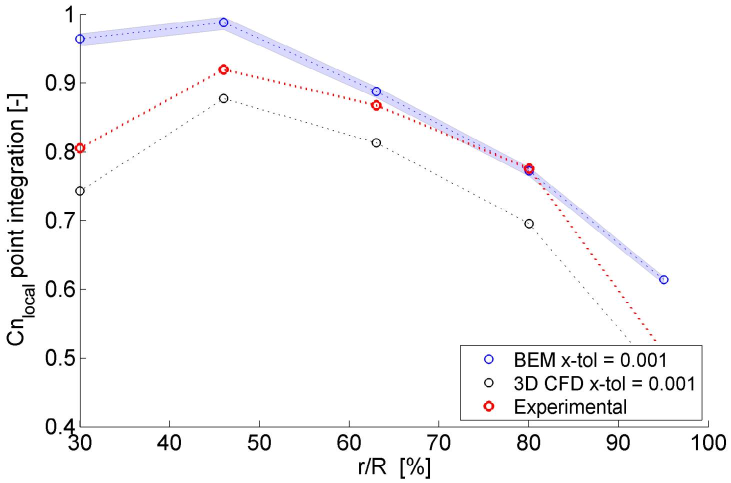

(a) The normal coefficient C_N at the sections at 30%, 46%, 63%, 80% and 95%

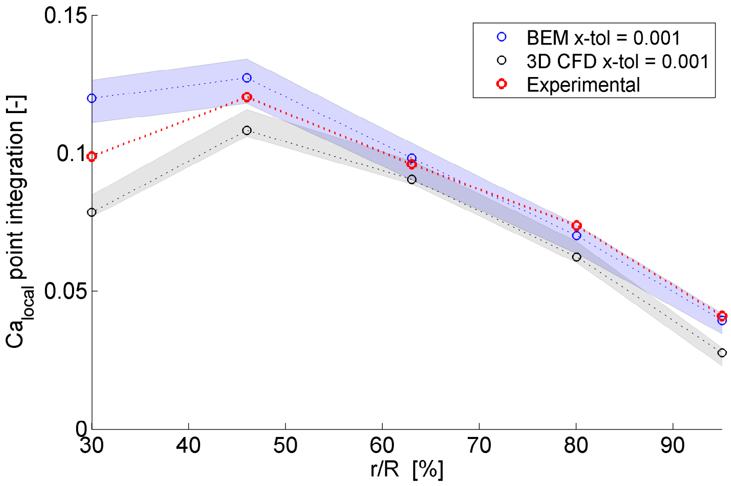

(a) The axial coefficient C_A at the sections at 30%, 46%, 63%, 80% and 95%

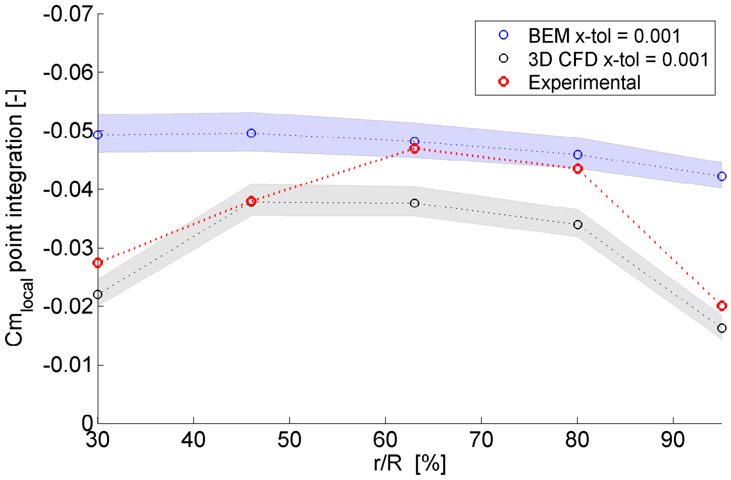

(b) The moment coefficient C_M at the sections at 30%, 46%, 63%, 80% and 95%

Figure 6.9: The different coefficients at the sections at 30%, 46%, 63%, 80% and 95% obtained by the different methods

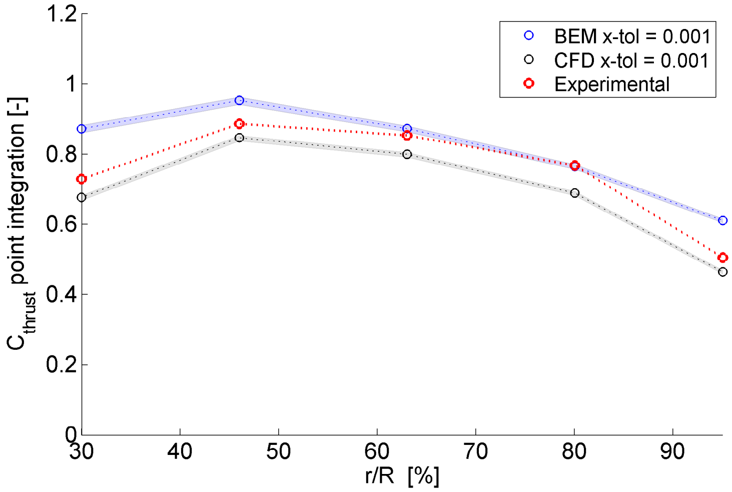

(a) The thrust coefficient at 30%, 46%, 63%, 80% and 95% of the blade

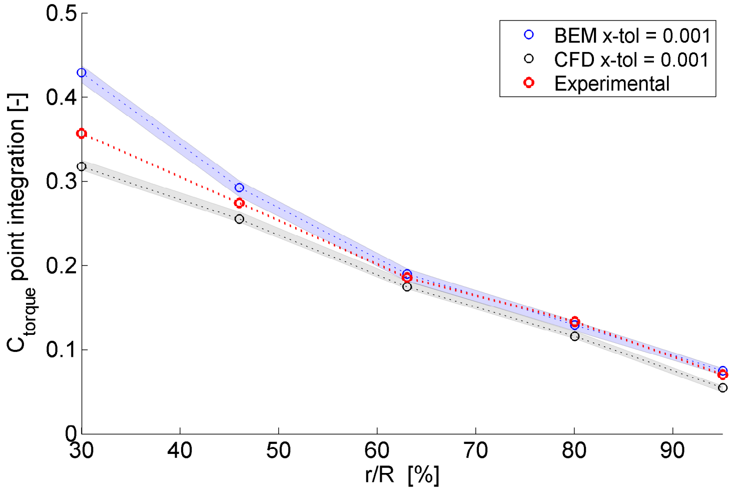

(b) The torque coefficient at 30%, 46%, 63%, 80% and 95% of the blade

Figure 6.10: The sensitivity of the torque and thrust

7 | Conclusion

In this report different prediction models for wind turbine aerodynamics are presented and discussed. The main purpose of this report was to compare a preliminary 2D BEM based method with 3D CFD simulations.

The results in chapter 6 show that the BEM method, which is one of the simplest and fastest methods, is able to make a good estimation of the total thrust and torque of a wind turbine operating at, or close to, the design conditions. For the test case the deviation is approximately 10 percent of the experimental values. Also the CFD result show good agreement with the experimental values. The fact that the CFD results under estimate the thrust and torque can probably be decreased by making the cells of the grid around the blade finer. But as a result this would increase the calculation time and costs of the simulations. The reason that the BEM method over predicts the thrust and torque can be attributed to the fact that the BEM doesn't account for tip and root losses. To increase the accuracy of the BEM method it is therefore wise to extend this method with a tower shadow model and a tip loss- or a wake model. The visualisation of the CFD results show that the flow around the middle part of the blade is mainly 2D, which clarifies why the results of the BEM method agrees so well with the measurements.

The comparison of the pressure integration shows that the main differences between the methods arise at the root and the tip where the 3D effects become stronger. From the sensitivity analysis in section 6.3.1. can be concluded that the results of the integration are highly dependent on the accuracy of the available data. This shows how important accurate data is for a fair comparison.

The main advantage of the BEM method is that it requires much less computational power than a CFD simulation while the results are still good. However the applicability of the BEM method is limited to wind turbines operating at, or close to, the design conditions while the CFD methods can predict the flow in a much wider range. When operating close to the design conditions, the BEM method gives a good approximation of the angles of incidence the blade experiences, but a great advantage of the CFD is that it is more easy to visualise the flow around the blades. This provides good insight in the flow behaviour around the blade which can be very valuable in the design process.

Bibliography

[1] O. Axelsson. *Iterative Solution Methods*. Cambridge University Press, Cambridge, MA, edition, 1994.

[2] B. Baldwin and H. Lomax. Thin-layer Approximation and Algebraic Model for Separated Turbulent Flows. In *AIAA 16th Aerospace Sciences Meeting, Huntsville, AL.*, January 16–18 1978.

[3] B. S. Baldwin and T. J. Barth. A One-Equation Turbulence Transport Model for High Reynolds Number Wall-Bounded Flows. Technical Memorandum NASA-TM-102847, NASA, August 1990.

[4] J. Boussinesq. *Théorie de l'Écoulement Tourbillonant et Tumultueux des Liquides dans des Lits Rectilignes à Grande Section, Tome I-II*. Gaulthier-Villars, Paris, France, first edition, 1897.

[5] T. Cebeci and A. M. O. Smith. *Analysis of Turbulent Boundary Layers*. Number 15. Applied Mathematics and Mechanics. Academic Press, New York, NY, 1974.

[6] P. Chassaing. *Turbulence en Mécanique des Fluides*. Cépaduès-Éditions, Toulouse, France, first edition, 2000.

[7] C.P. Chen. A Non-Isotropic Multiple-Scale Turbulence Model. Technical Report NASA-CR-184217, NASA, September 1990.

[8] T.J. Craft, B.E. Launder, and K. Suga. Development and Application of a Cubic Eddy-Viscosity Model of Turbulence. *International Journal of Heat and Fluid Flow*, 17(2):108–115, 1996.

[9] F. Dehaeze. *Aeroelastic Analysis of Turbulent Rotor Flows*. PhD thesis, January 2012.

[10] P. A. Durbin. Near-Wall Turbulence Closure Modeling without Damping Functions. *Theoretical and Computational Fluid Dynamics*, 3(1):1–13, 1991.

[11] K. Badcock G.N. Barakos, R. Steijl and A. Brocklehurst. Development of CFD Capabilty for Full Helicopter Engineering Analysis. pages 91.1–91.15. 31st European Rotorcraft Forum, September 2005.

[12] K. Hanjalić and B. E. Launder. A Reynolds Stress Model of Turbulence and its Application to Thin Shear Flows. *Journal of Fluid Mechanics*, 52:609–638, 1972.

[13] K. Hanjalic, B. E. Launder, and R. Schiestel. Multiple-Time-Scale Concepts in Turbulent Transport Modeling. In *Von Karman Institute for Fluid Dynamics Measurements and Predictions of Complex Turbulent Flows*, volume 1, 1980.

[14] F. H. Harlow and P. I. Nakayama. Turbulence Transport Equations. *Journal of Fluid Mechanics*, 10(11):2323–2332, 1967.

[15] A. Jameson. Time Dependent Calculations Using Multigrid, with Applications to Unsteady Flows Past Airfoils and Wings. In *10th Computational Fluid Dynamics Conference, Honolulu, HI*, 1991. AIAA-91-1596.

[16] D.A. Johnson and L.S. King. A Mathematically Simple Turbulence Closure Model for Attached and Separated Turbulent Boundary Layers. *AIAA Journal*, 23(11):1684–1692, November 1985.

[17] W.P Jones and B.E Launder. The Prediction of Laminarization with a Two-Equation Model of Turbulence. *International Journal of Heat and Mass Transfer*, 15(2):301–314, 1972.

[18] S.-W. Kim. Numerical Investigation of Separated Transonic Turbulent Flows with a Multiple-Time-Scale Turbulence Model. Technical Memorandum NASA-TM-102499, NASA, January 1990.

[19] M.A. Woodgate K.J. Badcock, B.E. Richards. Elements of Computational Fluid Dynamics on Block Structured Grids Using Implicit Solvers. *Progress in Aerospace Sciences*, 36:351–392, 2000.

[20] A.N. Kolmogorov. Equations of Turbulent Motion of an Incompressible Turbulent Fluid. *Izvestiya Akademii Nauk SSSR, Seriya Fizicheskaya*, 6(1–2):56–58, 1942.

[21] P. Malecki. *Étude de Modèles de Turbulence pour les Couches Limites Tridimensionnelles*. PhD thesis, ENSAE, Toulouse, France, 1994.

[22] F.R. Menter. Two-Equation Eddy-Viscosity Turbulence Models for Engineering Applications. *AIAA Journal*, 32(8):1598–1605, August 1994.

[23] S. Moir and A. Gould. VoTMATA — British Aerospace Default Model. Technical report, BAE SYSTEMS, 1998.

[24] M.V. Morkovin. Effects of Compressibility on Turbulent Flows. *Mécanique de la Turbulence*, 108:367–380, 2007. Coll. CNRS, CNRS, Paris.

[25] P. Nayyar and G. Barakos. A Summary of Turbulence Modelling Approaches in CFD. Aerospace Engineering Report 0206, University of Glasgow, September 2002.

[26] S. Osher and S. Chakravarthy. Upwind Schemes and Boundary Conditions with Applications to Euler Equations in General Geometries. *Journal of Computational Physics*, 50:447–481, January–February 1983.

[27] G.N. Barakos R. Steijl and K. Badcock. A Framework for CFD Analysis of Helicopter Rotors in Hover and Forward Flight. *International Journal for Numerical Methods in Fluids*, 51:819–847, January 2006.

[28] O. Reynolds. On the Dynamical Theory of Incompressible Viscous Fluids and the Determination of the Criterion. *Philosophical Transactions of the Royal Society of London*, A(186):123–164, 1895.

[29] P.L. Roe. Approximate Riemann Solvers, Parameter Vectors, and Difference Schemes. *Journal of Computational Physics*, 43(2):357–372, October 1981.

[30] J. G. Schepers. *Engineering Models in Wind Energy Aerodynamics*. PhD thesis, Delft University of Technology, The Netherlands, 2012.

[31] S.Gomez-Iradi, R. Steijl and G.N. Barakos. Development and Validation of a CFD Technique for the Aerodynamic Analysis of HAWT. *Journal of Solar Energy Engineering*, 131(3), 2009.

[32] T. P. Sommer, R. M. C. So, and H. S. Zhang. A Near-Wall Four-Equation Turbulence Model for Compressible Boundary Layers. Technical Report NASA-CR-4436, NASA, April 1992.

[33] Ph. Spalart. Strategies for Turbulence Modelling and Simulations. *International Journal of Heat and Fluid Flow*, 21(3):252–263, June 2000.

[34] Ph. Spalart and S.R. Allmaras. A One-Equation Turbulence Model for Aerodynamic Flows. *La Recherche Aérospatiale*, 1:5–21, 1994.

[35] D.B. Spalding. The Prediction of Two-Dimensional, Steady Turbulent Flows. Technical Report Heat Transfer Section Report EF/TN/A/16, Imperial College, 1969.

[36] C.G. Speziale and P.S. Bernard. The Energy Decay in Self-Preseving Isotropic Turbulence Revisited. *Journal of Fluid Mechanics*, 241:645–667, 1992.

[37] R. Steijl and G.N. Barakos. Sliding Mesh Algorithm for CFD Analysis of Helicopter Rotor Fuselage Aerodynamics. *International Journal for Numerical Methods in Fluids*, 58:527–549, February 2008.

[38] UK Research Councils. HECToR: UK National Supercomputing Service. http://www.hector.ac.uk/, 2007.

[39] B. van Leer. Flux-vector splitting for the euler equations. In *Eighth International Conference on Numerical Methods in Fluid Dynamics*, volume 170 of *Lecture Notes in Physics*, pages 507–512. Springer Berlin / Heidelberg, 1982.

[40] D.C. Wilcox. Multiscale Model for Turbulent Flows. *AIAA Journal*, 26(11):1311–1320, November 1988.

[41] D.C. Wilcox. Simulation of Transition with a Two-Equation Turbulence Model. *AIAA Journal*, 32(2):247–255, February 1994.

[42] M. Woodgate, K. Badcock, B. Richards, and R. Gatiganti. A Parallel 3D Fully Implicit Unsteady Multiblock CFD Code Implemented on a Beowulf Cluster. In *Parallel CFD 1999, Williamsburg, VA, USA*, 1999.

Appendix

A: Pressure integration moment coefficient

In this section the variation in the integrated moment coefficient of section 6.2 is investigated in more detail. The purpose of this section is to clarify the reason of the differences that appear in the pressure integration of the moment coefficient in section 6.2. Starting with the comparison of the experimental values of the pressure coefficient with the 2D CFD values obtained in combination with the BEM method. The C_p values of the first slice (at 30 % of the radius) are shown in Figure 7.1.

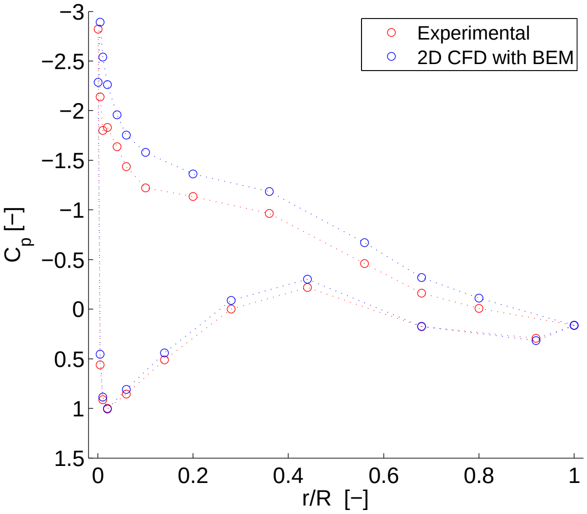

Figure 7.1: C_p values for $\frac{r}{R} = 30\%$

The integrated moment coefficients for this slice calculated in section 6.2 are:

$\mathrm{Cm}_{\mathrm{BEM}}$ = -0.4926
$\mathrm{Cm}_{\mathrm{exp}}$ = -0.02747
Deviation = -0.02179

From Figure 7.1 can be noticed that the main differences are situated at the upper surface. For this reason the upper surface is investigated in more detail in Figure 7.2, where the filled area represents the difference between the two pressure coefficients. The contribution of this difference to the moment coefficient is:

Deviation $\mathrm{Cm}_{\mathrm{up}}$: -0.023331
Total deviation : -0.02179

These values show that it is reasonable to assume that the main difference in the moment coefficient is caused by the upper surface. To check the reliability of this value a very rough estimation can be made with the help of Figure 7.2. Assume that the part up to 0.5 is more or less balanced around the quarter chord point and that the contribution of the part between 0.5 and 1 can be estimated by:

$$dC_p * dx * r = -0.1 * 0.5 * (0.75 - 0.25) = -0.025 \tag{7.1}$$

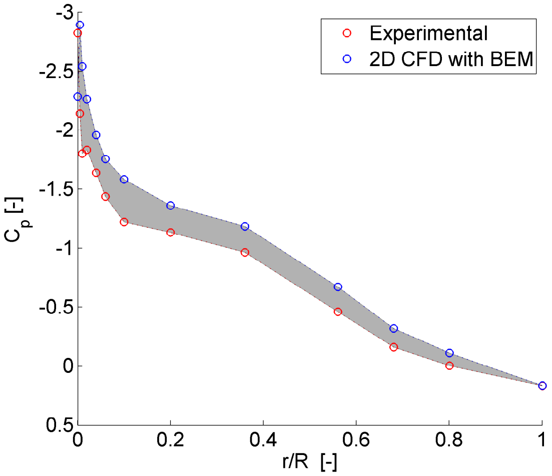

Figure 7.2: C_p difference upper surface

with C_p an estimation for the difference of the pressure coefficient, dx the surface and r an estimation for the average length to the quarter chord. This explanation shows why the moment coefficient can vary so much. The differences in the C_m values of the other slices can be clarified in a similar way.

From this analysis can be concluded that a little variation in the pressure coefficient can cause a big difference in the moment coefficient which means that the moment coefficient is very sensitive to little inaccuracies in the results.